UNIVERSIDAD POLITECNICA DE VALENCIA

ESCUELA POLITECNICA SUPERIOR DE GANDIA

I.T. Telecomunicación (Sist. de Telecomunicación)

"2.4 GHz MIMO Antenna on Microstrip Technology"

TRABAJO FINAL DE CARRERA

Autor/es:
Jesús Escrivá Muñoz

Director/es:
Ross, Murch

GANDIA, 2009

HONG KONG UNIVERSITY OF SCIENCE AND TECHNOLOGY

香港科技大學

Technical Telecommunications Engineering
Branch: Telecommunications Systems

2.4 GHz MIMO Antenna on Microstrip Technology

FINAL YEAR PROJECT

Author:
Jesús Escrivá Muñoz
Exchange Student from
Universitat Politènica de València - Spain

Supervisor/s:
Prof. Ross MURCH

HONG KONG, 2009

The following Final Year Project has been carried out in the Department of Electronic and Computer Engineering of the **Hong Kong University of Science and Technology** within the ***Promoe*** Exchange Program from the Escola Politècnica Superior de Gandia of the **Universitat Politècnica de Valencia.**

UNIVERSIDAD POLITECNICA DE VALENCIA

OFICINA DE PROGRAMAS INTERNACIONALES DE INTERCAMBIO

ACADEMIC CERTIFICATE FOR STUDENTS UNDER *PROMOE* PROGRAMME 2008-09

Host University:___**Hong Kong University of Science and Technology**_____

Country:_____**Hong Kong (SAR PRC)**_____

Mr./Mrs./Dr **Murch, Ross** from the above Institution,

HEREBY CERTIFIES:

that the Stutent **Jesús Escrivá Muñoz** under the INTERUNIVERSITY EXCHANGE AGREEMENT, from **Escola Politècnica Superior de Gandia** of the UNIVERSITAT POLITÈCNICA DE VALÈNCIA, has carried out at this Institution during the Spring semester (January – May 2008), his **Final Year Project** obtaining a **final grade of ____ out of 10 points.**

On the _____, of May 2009

Signature and Stamp of the Host Institution

INDEX

2.4 GHz MIMO Antenna on Microstrip Technology

Abstract

In this work, we have analyzed triangular and rectangular microstrip patches and their use in MIMO communication systems. Triangular patches have demonstrated a great capability of miniaturization due to its geometrical shape. Etching some slots in the patches changes the antenna frequency response so that dual-band and broadband designs are easily conceived. Several configurations are analyzed using the *HFSS* simulation software and a 2.4 GHz four-port MIMO antenna is fabricated on a FR-4 substrate. Simulation results and some graphics are also included.

CHAPTER I. INTRODUCTION

Wireless Com.

Nowadays the most pressing problems in Wireless Communications are spectral efficiency and interference, problems which are expected to increase its importance in the near future. Wireless Internet, mobile video and data communication will push the spectrum to its limitations. In the same way interference with other services will be increased by the extending use of spectrum. A typical candidate for interference in both directions is, for example, Ultra-Wide-Band. Taking this into the account the most prominent task for communication scientists is to increase the spectral efficiency and to introduce measures for interference reduction.

Smart antenna systems are certainly revolutionizing the communications systems [1]. So far, only the spectrum, the time and the code domain had been exploited for communications systems. The resources spectrum and code are very limited. Smart antennas exploit the spatial domain, which has been almost completely unused so far. For multiplex transmission within one communications link, i.e. a parallel transmission of several data streams at the same time and frequency only separated by the spatial domain, multiple transmit and multiple receive antennas are required. MIMO systems (Multiple Input Multiple Output) promise to reach very large data rates and therewith high spectral efficiencies.

Impairments in Wireless Channels

Communication in wireless channels is impaired predominantly by multi-path fading. Multi-path is the arrival of the transmitted signal at an intended receiver through differing angles and/or differing time delays and/or differing frequency shifts due to the scattering of electromagnetic waves in the environment. Consequently, the received signal power fluctuates in space (due to angle spread) and/or frequency (due to delay spread) and/or time (due to Doppler spread) through the random superposition of the impinging multi-path components. This random fluctuation in signal level, known as fading, can severely affect the quality and reliability of wireless communication. Additionally, the constraints posed by limited power and scarce frequency bandwidth make the task of designing high data rate, high reliability wireless communication systems extremely challenging.

MIMO Technology

MIMO technology constitutes a breakthrough in wireless communication system design. The technology offers a number of benefits that help meet the challenges posed by both the impairments in the wireless channel (multi-path and fading) as well as resource constraints. In addition to the time and frequency dimensions that are exploited in conventional single-antenna (single-input single-output) wireless systems, the leverages of MIMO are realized by exploiting the spatial dimension (provided by the multiple antennas at the transmitter and the receiver) [2].

Therefore, the use of multiple antennas at the transmitter and receiver in wireless systems has rapidly gained in popularity over the past decade due to its powerful capabilities of enhancing the communication system performance.

Benefits of MIMO Technology

We can observe in Figure 1.1 the expected performance gains from the use of MIMO technology by plotting the data rate versus the receive signal-to-noise ratio (SNR) in a 100 kHz channel for an M×M (i.e., M receive and M transmit antennas) fading link with M=1, 2, 4. Assuming a target receives SNR of 25 decibels (dB), a conventional single-input single-output (i.e., M=1) system can deliver a data rate of 0.7 Mbps (where Mbps denotes Mbits per second). With M=2 and 4 we can realize data rates of 1.4 and 2.8 Mbps respectively. This increase in data rate is realized for no additional power or bandwidth expenditure compared to the single-input single-output system.

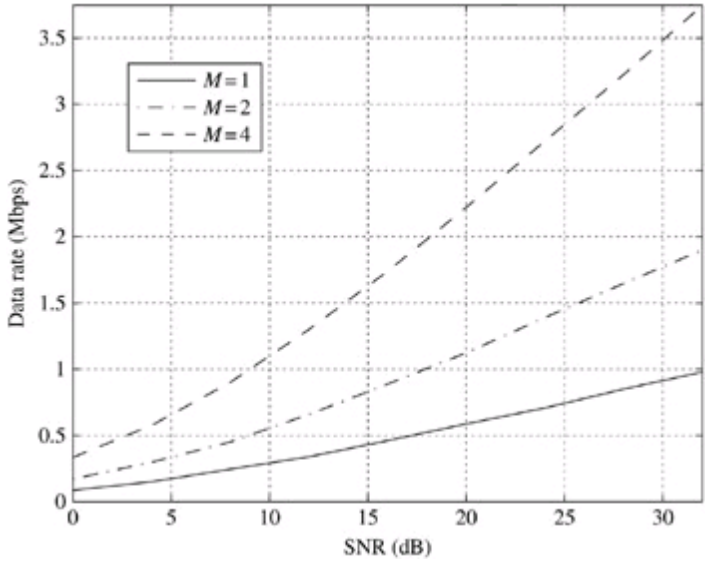

Figure 1.1

Fig. 1.1: Average data rate versus SNR for different antenna configurations.

The benefits of MIMO technology that help achieve such significant performance gains are array gain, spatial diversity gain, spatial multiplexing gain and interference reduction. These gains are described in brief below.

Array gain. That is the increase in receive SNR that results from a coherent combining effect of the wireless signals at a receiver. The coherent combining may be realized through spatial processing at the receive antenna array and/or spatial pre-processing at the transmit antenna array. Array gain improves resistance to noise, thereby improving the coverage and the range of a wireless network.

Spatial diversity gain. As mentioned earlier, the signal level at a receiver in a wireless system fluctuates or fades. Spatial diversity gain mitigates fading and is realized by providing the receiver with multiple (ideally independent) copies of the transmitted signal in space, frequency or time. With an increasing number of independent copies (the number of copies is often referred to as the diversity order), the probability that at least one of the copies is not experiencing a deep fade increases, thereby improving the quality and reliability of reception. A MIMO channel with Mtx transmit antennas and Mrx receive antennas potentially offers Mtx x Mrx independently fading links, and hence a spatial diversity order of Mtx x Mrx.

Spatial multiplexing gain. MIMO systems offer a linear increase in data rate through spatial multiplexing, i.e., transmitting multiple, independent data streams within the bandwidth of operation. Under suitable channel conditions, such as rich scattering in the environment, the receiver can separate the data streams. Furthermore, each data stream experiences at least the same channel quality that would be experienced by a single-input single-output system, effectively enhancing the capacity by a multiplicative factor equal to the number of streams. In general, the number of data streams that can be reliably supported by a MIMO channel equals the minimum of the number of transmit antennas and the number of receive antennas, i.e., min{MT, MR}. The spatial multiplexing gain increases the capacity of a wireless network.

Interference reduction and avoidance. Interference in wireless networks results from multiple users sharing time and frequency resources. Interference may be mitigated in MIMO systems by exploiting the spatial dimension to increase the separation between users. For instance, in the presence of interference, array gain increases the tolerance to noise as well as the interference power, hence improving the signal-to-noise-plus-interference ratio (SINR). Additionally, the spatial dimension may be leveraged for the purposes of interference avoidance, i.e., directing signal energy towards the intended user and minimizing interference to other users. Interference reduction and avoidance improve the coverage and range of a wireless network.

In general, it may not be possible to exploit simultaneously all the benefits described above due to conflicting demands on the spatial degrees of freedom. However, using some combination of the benefits across a wireless network will result in improved capacity, coverage and reliability.

Situation of MIMO Technology

The potential to provide the next major leap forward for wireless communications has led this technology to becoming the next frontier of wireless communications. As a result, it has received the attention not only of the international research and development community, but also of the wireless communications industry. This is evidenced from the international standardization efforts in the context of UMTS (e.g., 3GPP) and IEEE 802.11 (for wireless LANs) and also in the context of proposals for next generation (4G and beyond) wireless systems [4].

For example, the third-generation cellular system specification (3GPP) currently supports only an optional two antenna space-time transmit diversity scheme and does not require the handsets to have more than one antenna element [3]. Sophisticated techniques that employ spatial multiplexing or support more antenna elements have met with considerable opposition in 3GPP. While the adoption of MIMO has made headway in the next-generation wireless local area network (WLAN) standard IEEE 802.11n, which aims to transfer raw information at rates greater than 100 Mbps over a 20-MHz bandwidth, complexity considerations are likely to make the adopted MIMO scheme an elementary one that supports a small number of antenna elements.

In this report, we aim to design and construct a MIMO antenna for wireless communications by using microstrip technology. In Chapter II, the theoretical aspects of MIMO communication systems are reviewed. Afterwards, in Chapter III we find an introduction to the microstrip antenna patch technology and a study of the rectangular and the triangular patch is carried out. In Chapter IV, the former theoretical introduction allows us to design a single broadband triangular patch antenna by using slots. This structure is used in Chapter V for the MIMO antenna, whose performance is then analyzed.

CHAPTER II. MIMO WIRELESS COMMUNICATION SYSTEMS

This chapter introduces the principles of MIMO systems employing the necessary mathematical analysis to consider the achieved capacity performance.

The mathematical representation of the MIMO system is performed through a complex matrix, which depends on the scenario considered each time. The capacity achieved by the MIMO channel in all the above cases is studied with the use of the Shannon extended capacity formula. The capacity performance results, developed from the simulations performed, are related to the number of the multiple antenna elements that the receiver and the transmitter are equipped with, the distance between them and the degree of correlation evidenced [4].

2.1 Shannon's Capacity Formula

Shannon's capacity formula approximated theoretically the maximum achievable transmission rate for a given channel with bandwidth B, transmitted signal power P and single side noise spectrum N_0, based on the assumption that the channel is white Gaussian (i.e., fading and interference effects are not considered explicitly).

$$C = B\log(1+\frac{P}{N_0 B}) \qquad \text{Equation 2.1}$$

In practice, this is considered to be a SISO scenario (single input, single output) and Equation 2.1 gives an upper limit for the achieved error-free SISO transmission rate. If the transmission rate is less than C bps, then an appropriate coding scheme exists that could lead to reliable and error-free transmission. On the contrary, if the transmission rate is more than C bps, then the received signal, regardless of the robustness of the employed code, will involve bit errors.

2.2 Extended Capacity Formula for MIMO Channels

For the case of multiple antennas at both the receiver and the transmitter ends, the channel exhibits multiple inputs and multiple outputs and its capacity can be estimated by the extended Shannon's capacity formula, as described below.

2.2.1 General Capacity Formula

We consider an antenna array with n_t elements at the transmitter and an antenna array with n_r elements at the receiver. The impulse response of the channel between the *j*-th transmitter element and the *i*-th receiver element is denoted as $h_{i,j}(\tau, t)$. The MIMO channel can then be described by the $n_r \times n_t$ $\mathbf{H}(\tau, t)$ matrix:

$$\mathbf{H}(\tau,t) = \begin{bmatrix} h_{1,1}(\tau,t) & h_{1,2}(\tau,t) & \cdots & h_{1,n_t}(\tau,t) \\ h_{2,1}(\tau,t) & h_{2,2}(\tau,t) & \cdots & h_{2,n_t}(\tau,t) \\ \vdots & \vdots & \ddots & \vdots \\ h_{n_r,1}(\tau,t) & h_{n_r,2}(\tau,t) & \cdots & h_{n_r,n_t}(\tau,t) \end{bmatrix}$$

Equation 2.2

The matrix elements are complex numbers that correspond to the attenuation and phase shift that the wireless channel introduces to the signal reaching the receiver with delay τ. The input-output notation of the MIMO system can now be expressed by the following equation:

$$\mathbf{y}(t) = \mathbf{H}(\tau,t) \otimes \mathbf{s}(t) + \mathbf{u}(t)$$

Equation 2.3

where $\otimes$ denotes convolution, $\boldsymbol{s}(t)$ is a $n_t \times 1$ vector corresponding to the n_t transmitted signals, $\mathbf{y}(t)$ is a $n_r \times 1$ vector corresponding to the n_r received signals and $\mathbf{u}(t)$ is the additive white noise.

If we assume that the transmitted signal bandwidth is narrow enough that the channel response can be treated as flat across frequency, then the discrete-time description corresponding to Equation 2.3 is

$$\mathbf{r}_\tau = \mathbf{H}\mathbf{s}_\tau + \mathbf{u}_\tau$$

Equation 2.4

Although an estimation of the capacity of a MIMO channel is possible, we can also perform linear transformations at both the transmitter and receiver converting the MIMO channel to $n = \min(n_r, n_t)$ SISO subchannels (given that the channel is linear) and, hence, reach more insightful results. The former estimation proved in [5,6] is as follows

$$C = \log_2[\det(\mathbf{I} + \mathbf{H}\mathbf{R}_{ss}\mathbf{H}^H)]$$

Equation 2.5

where $\mathbf{H}$ is the $n_r \times n_t$ channel matrix, $\mathbf{R}_{ss}$ is the covariance matrix of the transmitted vector $\mathbf{s}$, $\mathbf{H}^H$ is the transpose conjugate of the $\mathbf{H}$ matrix and p is the maximum normalized transmit power.

2.2.2 Transformation of the MIMO Channel into n SISO Subchannels

Every matrix $\mathbf{H} \in \mathbb{C}^{n_r \times n_t}$ can be decomposed accordingly to its singular values. Suppose that for the aforementioned channel matrix this transformation is given by Equation 2.6.

$$\mathbf{H} = \mathbf{U}\mathbf{D}\mathbf{V}^H$$

Equation 2.6

where the matrices **U**, **V** are unitaries of dimensions $n_r \times n_r$ and $n_t \times n_t$ accordingly, while **D** is a non-negative diagonal matrix of dimensions $n_r \times n_t$. The diagonal elements of matrix **D** are the singular values ε of the channel matrix **H**.

The operations that lead to the linear transformation of the channel into $n = \min(n_r, n_t)$ SISO subchannels are described as follows: First, the transmitter multiplies the signal to be transmitted **x** with the matrix **V**, the receiver multiplies the received signal **r** and noise with the conjugate transpose of the matrix **U** as follows:

$$\mathbf{s}_\tau = \mathbf{V} \cdot \mathbf{x}_\tau \quad \text{Equation 2.7}$$

$$\mathbf{y}_\tau = \mathbf{U}^H \cdot \mathbf{r}_\tau \quad \text{Equation 2.8}$$

$$\mathbf{n}_\tau = \mathbf{U}^H \cdot \mathbf{u}_\tau \quad \text{Equation 2.9}$$

Substituting Equation 2.4 into Equation 2.8 gives:

$$\mathbf{y}_\tau = \mathbf{U}^H \cdot \mathbf{r}_\tau \overset{(2.2)}{\Longrightarrow} \mathbf{y}_\tau = \mathbf{U}^H\mathbf{H}\mathbf{s}_\tau + \mathbf{U}^H\mathbf{u}_\tau \overset{(2.2)}{\Longrightarrow} \mathbf{y}_\tau = \mathbf{U}^H\mathbf{H}\mathbf{V}\mathbf{x}_\tau + \mathbf{n}_\tau \overset{(2.2)}{\Longrightarrow} \mathbf{y}_\tau$$
$$= \mathbf{U}^H\mathbf{U}\mathbf{D}\mathbf{V}^H\mathbf{V}\mathbf{x}_\tau + \mathbf{n}_\tau$$

Since **U** and **V** are unitary matrices, they satisfy $\mathbf{U}^H\mathbf{U} = \mathbf{I}_{n_r}, \mathbf{V}^H\mathbf{V} = \mathbf{I}_{n_t}$ hence:

$$\mathbf{y}_\tau = \mathbf{D}\mathbf{x}_\tau + \mathbf{n}_\tau \quad \text{Equation 2.10}$$

Each component of the received vector y can be written as:

$$y_\tau^k = \varepsilon_k x_\tau^k + n_\tau^k \quad \text{Equation 2.11}$$

where ε_k are the singular values of matrix **H** according to the transformation that took place above.

It was proven in [1] that the total capacity of n SISO subchannels is the sum of the individual capacities and as a result the total MIMO capacity is:

$$C = \sum_{k=1}^{n} \log_2(1 + p_k \varepsilon_k^2) \quad \text{Equation 2.12}$$

where p_k is the power allocated to the *k*th subchannel and ε_k^2 is its power gain. We notice that according to the singular value decomposition algorithm $\varepsilon_k^2, k = 1,2,\dots,n$ are the eigenvalues of the $\mathbf{H}\mathbf{H}^H$ matrix, which are always non-negative. Furthermore, regardless of the power allocation algorithm used, p_k must satisfy

$$\sum_{k=1}^{n} p_k < p \quad \text{Equation 2.13}$$

because of the wanted power constraint.

At this point, there are two cases of particular interest that need further consideration: the knowledge (or not) by the transmitter of the Channel State Information (CSI).

2.2.3 No CSI at the Transmitter

Considering Equation 2.12, we notice that the achieved capacity depends on the algorithm used for allocating power to each subchannel. The theoretical analysis assumes the channel state known at the receiver. This assumption stands correct since the receiver usually performs tracking methods in order to obtain CSI, however the same consideration does not apply to the transmitter. When the channel is not known at the transmitter, the transmitting signal $\boldsymbol{s}$ is chosen to be statistically non-preferential, which implies that the n_t components of the transmitted signal are independent and equi-powered at the transmit antennas. Hence, the power allocated to each of the n_t subchannels is $p_k = p/n_t$. Applying the last expression to Equation 2.5 gives:

$$C = \log_2\left[\det\left(\mathbf{I} + \frac{p}{n_t}\mathbf{H}\mathbf{H}^H\right)\right] \quad \text{Equation 2.14}$$

or

$$C = \sum_{k=1}^{n} \log_2\left(1 + \frac{p}{n_t}\varepsilon_k^2\right) \quad \text{Equation 2.15}$$

2.2.4 CSI at the Transmitter

In cases in which the transmitter has knowledge of the channel, it can perform optimum combining methods during the power allocation process. In that way, the SISO subchannel that contributes to the information transfer the most is supplied with more power.

One method to calculate the optimum power allocation to the *n* subchannels is to employ the water-pouring algorithm (a detailed discussion of this algorithm can be found in [7]).

Considering the assumption of CSI at the transmitter, we can proceed to the following capacity formula.

$$C = \sum_{k=1}^{n} \log_2\left(1 + \frac{\gamma_k p}{n_t}\varepsilon_k^2\right) \quad \text{Equation 2.16}$$

The difference between Equation 2.14 and Equation 2.15 is the coefficient γ_k that corresponds to the amount of power that is assigned to the *k*th subchannel. This coefficient is given by:

$$\gamma_k = E\{|s_k|^2\} \quad \text{Equation 2.17}$$

and satisfies the constraint

$$\sum_{k=1}^{n} \gamma_k = n_t$$ Equation 2.18

The goal with the water-pouring algorithm is to find the optimum $\gamma_k$that maximizes the capacity given in Equation 2.15.

2.2.5 Channel Estimation at the Transmitter

As mentioned earlier, the CSI is not usually available at the transmitter. In order for the transmitter to obtain the CSI, two basic methods are used: the first is based on feedback and the second on the reciprocity principle.

In the first method the forward channel is calculated by the receiver and information is sent back to the transmitter through the reverse channel. This method does not function properly if the channel is changing fast. In that case, in order for the transmitter to get the right CSI, more frequent estimation and feedback are needed. As a result, the overhead for the reverse channel becomes prohibitive. According to the reciprocity principle, the forward and reverse channels are identical when the time, frequency and antenna locations are the same. Based on this principle the transmitter may use the CSI obtained by the reverse link for the forward link. The main problem with this method emerges when frequency duplex schemes are employed.

2.3 Remarks on the Extended Shannon Capacity Formula

In this section we will present the theoretical upper and lower bounds of MIMO capacity. The algebraic expressions and assumptions considered here were first derived in [1]. After this, the best case for the MIMO capacity will be analyzed and the concept of the effective degrees of freedom will be introduced.

2.3.1 Bounds on MIMO capacity

Since the channel is submitted to Rayleigh fading, the channel matrix $\mathbf{H}$ is given by$\mathbf{H}_W$, which is referred to as spatially white matrix. The elements of $\mathbf{H}_W$ can be modeled as zero mean circularly symmetric complex Gaussian (ZMCSCG) random variables. The $\mathbf{H}_W$ has particular statistical properties that can be found in [7, 8].

We consider the transformation $\mathbf{H}_W = \mathbf{QR}$, where $\mathbf{Q}$ is a unitary and $\mathbf{R}$ is an upper-triangular matrix. This tranformation is referred to as Householder Transformation. According to this transformation the elements of $\mathbf{R}$ above the main diagonal are statistically independent, while the magnitude of the main diagonal entries are chi-squared distributed with $2n_r$, $2(n_r - 2 + 1), \ldots, 2(n_r - n_t + 1)$ degrees of freedom.

Using this, the lower capacity bound corresponds to:

$$C \geq \sum_{l=1}^{n_t} \log_2\left(1 + \frac{p}{n_t}\left|R_{l,l}\right|^2\right)$$ Equation 2.19

This equation practically shows that this bound is defined by the sum of the capacities of n_t independent subchannels with power gains that follow the chi-square distribution with $2n_r$, $2(n_r - 2 + 1), \ldots, 2(n_r - n_t + 1)$degrees of freedom.

The upper bound of the capacity is the sum of the capacities of n t independent subchannels, with power gains chi-squared distributed and with degrees of freedom $2(n_r + n_t - 1), 2(n_r + n_t - 3), \ldots, 2(n_r - n_t + 1)$. The difference of the mean values of the upper and lower bounds is less than 1b/s/Hz.

$$C \leq \sum_{l=1}^{n_t} \log_2\left[1 + \frac{p}{n_t}\left(\left|R_{l,l}\right|^2 + \sum_{m=l+1}^{n_t}\left|R_{l,m}\right|^2\right)\right]$$ Equation 2.20

2.3.2 Capacity of Orthogonal Channels

It is interesting to study the case where the capacity of the MIMO channel is maximized. We consider the simple case of $n_r = n_t = n$, along with a fixed total power transfer through the SISO subchannels (i.e., $\sum_{k=1}^{n} \varepsilon_k^2 = a$, where a is a constant). The capacity in Equation 2.14 is concave in the variables ε_k^2 and, as a result, it is maximized when $\varepsilon_k^2 = a/n$. The last equation reveals that the $\boldsymbol{H}^H\boldsymbol{H}$ matrix has n equal eigenvalues. Hence, $\mathbf{H}$ must be an orthogonal matrix, i.e., $\boldsymbol{H}^H = \mathbf{H}^{\mathrm{H}}\mathbf{H} = (a/n)\mathbf{I}_{\mathrm{n}}$. Therefore:

$$C = \log_2\left[\det\left(\mathbf{I} + \frac{pa}{n^2}\mathbf{I}_n\right)\right] \Leftrightarrow C = n \cdot \log_2\left(1 + \frac{pa}{n^2}\right)$$ Equation 2.21

If the matrix $\mathbf{H}$ satisfies $\mathbf{H}\mathbf{H}^H = n\mathbf{I}_n$, hence, Equation 2.13 becomes:

$$C = \log_2\left[\det\left(\mathbf{I} + \frac{p}{n}n\mathbf{I}_n\right)\right] \Leftrightarrow C = n \cdot \log_2(1 + p)$$ Equation 2.22

The last equation indicates that the capacity of an orthogonal MIMO channel is n times the capacity of the SISO channel.

2.3.3 Effective Degrees of Freedom

Based on Equation 2.14, we can assume that in high SNR regime, capacity can increase linearly with n. Specifically, for high SNR regime $(\varepsilon_k^2 p/n) \gg 1$ Equation 2.14 becomes:

$$C \approx \sum_{k=1}^{n} \log_2\left(\frac{p}{n}\varepsilon_k^2\right)$$ Equation 2.23

However, this assumption is not always confirmed. For some subchannels $(\varepsilon_k^2 p/n)$ is much smaller than one, and as a result the information transferred by these channels is nearly zero. This phenomenon is present in at least three cases:

- when the transmission is serviced through a low-powered device
- when there is a long-range communication application
- when there is strong fading correlation between subchannels

In the last case, the fading induced to a certain subchannel may cause the minimization of its corresponding ε_k^2.

In practice, the aforementioned cases are very likely to happen, therefore, the concept of EDoF is introduced. Intuitively, the EDoF value corresponds to the number of subchannels that actually contribute to the information transfer. In a more mathematical approach, the EDoF value indicates the non-zero singular values of the channel matrix H. A more detailed description of the EDoF can be found in [5].

2.4 Capacity of SIMO — MISO Channels

Single input, multiple output (SIMO) and multiple input, single output (MISO) channels are special cases of MIMO channels. In this paragraph we discuss the capacity formulas for the case of SIMO and MISO channels. We will consider $|h_i|^2 = 1$ then $\varepsilon_1^2 = n_r$ or n_t depending on SIMO or MISO analysis.

For a SIMO channel $n_t = 1, \text{so } n = \min(n_t, n_r) = 1$; hence, the CSI at the transmitter does not affect the SIMO channel capacity:

$$C_{SIMO} = \log_2(1 + p \cdot \varepsilon_1^2) = \log_2(1 + p \cdot n_r) \quad \text{Equation 2.24}$$

For a MISO channel $n_r = 1, \text{so } n = \min(n_t, n_r) = 1$. With no CSI at the transmitter, the capacity formula can be expressed as:

$$C_{MISO} = \log_2\left(1 + \frac{p}{n_t} \cdot \varepsilon_1^2\right) = \log_2(1 + p) \quad \text{Equation 2.25}$$

Comparing Equation 2.24 and Equation 2.25 we can see that $C_{SIMO} > C_{MISO}$. This is because the transmitter, as opposed to the receiver, cannot exploit the antenna array gain since it has no CSI and, as a result, cannot retrieve the receiver's direction.

2.5 Stochastic Channels

In order to use the aforementioned capacity formulas, it is necessary to obtain the channel matrix expression. There are many spatial channel models that are used for this purpose. In most cases, the simulations usually consider a stochastic channel approach, mainly the Rayleigh and the Rice models are used.

Consequently, under the stochastic channel consideration, the capacity achieved becomes a random variable, and in order to study its behavior, we use stochastic quantities, as described below.

2.5.1 Ergodic Capacity

The ergodic capacity of a MIMO channel is the ensemble average of the information rate over the distribution of the elements of the channel matrix **H**, and it is given by:

$$\bar{C} = E\{I\}$$ Equation 2.26

When there is no CSI at the transmitter, we can substitute Equation 2.13 into Equation 2.26, so the ergodic capacity is given by

$$\bar{C} = E\left\{\log_2\left[\det\left(\mathbf{I} + \frac{p}{n_t}\mathbf{H}\mathbf{H}^H\right)\right]\right\}$$ Equation 2.27

Whereas with CSI at the transmitter we use Equation 2.15, and the ergodic capacity is given by:

$$\bar{C} = E\left\{\sum_{k=1}^{n}\log_2\left(1 + \frac{\gamma_k p}{n_t}\varepsilon_k^2\right)\right\}$$ Equation 2.28

2.6 MIMO Capacity and Channel Models

It is the radio propagation channel that determines crucially the characteristics of the entire MIMO system [10]. Therefore, accurate modeling of MIMO channels is an important requisite for MIMO system design, simulation, and deployment. Moreover, the multidimensional statistical behavior of the MIMO fading channel is of foremost significance to the system performance (e.g., the influence of the spatial fading correlation). Therefore, it is important for the designer of a MIMO communication system to have an appropriate MIMO channel simulation model.

There are many different channel models. When the wireless environment is characterized by strong multipath activity, then the received signal follows the Rayleigh distribution. However, in other cases when the location of buildings leads to the street waveguide propagation phenomenon, and in areas near the base station where a line of sight (LOS) component may dominate, the Ricean distribution is more suitable. The receiver in that scenario "sees" a dominant signal component along with lower power components caused by multipath. The dominant component that reaches the receiver may not be the result of LOS propagation, e.g., the dominant component may be the mean value of strong multipaths caused by large scatterers.

Both before-mentioned channels are stochastic narrowband MIMO channel models. However, we should keep in mind the existence of a large diversity of models: both deterministic, such as the recorded impulse response and ray-tracing techniques, and stochastic (Ricean, Rayleigh, parametric, correlation based…).

CHAPTER III. MICROSTRIP ANTENNA TECHNOLOGY

In this section, we deal with the microstrip antenna technology which will be used for our MIMO antennas design. We present the basis of microstrip technology to finally tackle the analysis of rectangular and triangular microstrip patches.

The challenge for radiofrequency engineers is mainly to understand the complex systems starting with the transmitter and ending with the receiver. It is not enough to investigate only single components of the communications link. The antennas are an integral part of the MIMO system. MIMO systems exploit the multipath structure of the propagation channel. The antennas are adapted to the propagation channel. Correlations among channel coefficients are influenced by the antenna properties. As the antennas are collocated in a MIMO array, mutual coupling effects may occur. All these effects should be considered when designing an antenna array for MIMO systems.

Therefore, a major concern in MIMO systems is the integration of several antennas into small handheld devices. Finding feasible antenna configurations is an integral part of enabling the MIMO technology.

Background of Microstrip Antennas

Microstrip geometries which radiate electromagnetic waves were originally contemplated in the 1950's where size, cost, performance, ease of installation, and aerodynamic profile were constraints, such as in the case of high-performance aircrafts, spacecrafts, satellites and missile applications. Presently, there are other government and commercial applications, such as mobile radio and wireless communications, which have similar specifications.

The realization of radiators which are compatible with microstrip transmission line is nearly contemporary with its introduction in 1952 by Grieg and Englemann [11]. The earliest known realization of a microstrip like antenna integrated with microstrip transmission line was developed in 1953 by Déschamps [12]. By 1955 Gutton and Baissinot patented a microstrip antenna design [13].

Although there are many different varieties of microstrip patch antennas (MSPA), their common feature is that they basically consist of four parts (Figure 1.1):

- A very thin flat metallic region often called the *patch;*
- A *dielectric substrate;*
- A *ground plane,* which is usually larger than the patch; and
- A *feed,* which supplies the element power.

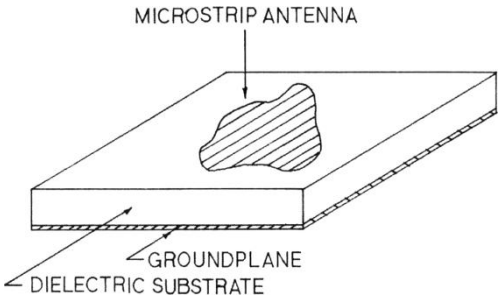

Figure 3.1

Figure 3.1 Typical MSPA

The reasons why this class of antennas has become so popular include the following [14-15]:

Characteristics of MSPA

- They are low-profile antennas.
- They are easily conformable to non planar surfaces.
- They are easy and inexpensive to manufacture in large quantities using modern printed-circuit techniques.
- When mounted to a rigid surface, they are mechanically robust.
- They can be designed to produce a wide variety of patterns and polarizations, depending on the mode excited and the particular shape of patch used.
- Other microwave devices realizable in microstrip may be integrated with a microstrip antenna with no extra fabrication steps (e.g. branch-line hybrid to produce circular polarization or corporate feed network for an array of microstrip antennas).

Disadvantages of the original microstrip antenna configurations include narrow bandwidth, spurious feed radiation, poor polarization purity, limited power capacity, and tolerance problems. Much of the development work in microstrip antennas has thus gone into trying to overcome these problems, in order to satisfy increasingly stringent systems requirements. This effort has involved the development of novel microstrip antenna configurations, and the development of accurate and versatile analytical models for the understanding of the inherent limitations of microstrip antennas, as well as for their design and optimization.

Applications of MSPA

A large number of commercial needs are met by the use of microstrip and printed antennas. The most popular microstrip antenna is certainly the rectangular patch. The **Global Positioning System** (GPS) has become ubiquitous in its applications. GPS applications such as the asset tracking of vehicles as well as marine use have created a large demand for antennas. The majority of these are rectangular patches which have been modified to produce right hand circular polarization (RHCP) and operate at 1.575 GHz. Numerous vendors offer patches designed using ceramics with a high dielectric constant (ε = 6, 20, 36) to reduce the rectangular microstrip antenna to as small a footprint as possible for a given application. The patches are provided ready for circuit board integration with low noise amplifiers. Rectangular patch antennas are also used for Bluetooth automotive applications (2.4GHz) with RHCP.

In recent years **Satellite Digital Audio Radio Services** (SDARS) have become a viable alternative to AM and FM commercial broadcasts in automobiles. The system has strict radiation pattern requirements which have been met with a combination of a printed monopole and TM_{21} mode annular microstrip antenna which has been altered with notches to produce left hand circular polarization at 2.338 GHz [16].

Wireless Local Area Networks (WLAN) provide short range high-speed data connections between mobile devices (such as a laptop computer) and wireless access points. The range for wireless data links is typically around 100 to 300 feet indoors and 2000 feet outdoors. Wireless data links use the IEEE Standards 802.11a,b,g. The majority of WLANs use the

unlicensed 2.4 GHz band (802.11b and 802.11g). The 802.11a standard uses the 5 GHz unlicensed frequency band. We can find several variations of the WLAN antenna such as multiband printed antennas which are integrated into ceiling tiles use a microstrip diplexer to combine the signal from GSM cell phones (860 MHz band), PCS cell phones (1.92 GHz band) and 802.11a wireless LAN service (2.4 GHz band) provided by two integrated microstrip dipoles [17].

3.1 Rectangular Microstrip Patch Antennas

Geometry of Rectangular MSPA

The rectangular microstrip patch antenna (RMSPA) is by far the most widely used configuration. Figure 3.2 shows the geometry of this antenna type. A rectangular metal patch of width $W = a$ and length $L = b$ is separated by a dielectric material from a ground plane by a distance *h*. The two ends of the antenna (located at 0 and *b*) can be viewed as radiating edges due to fringing fields along each edge of width $W = a$. The two *radiating edges* are separated by a distance $L = b$. The two edges along the sides of length *L* are often referred to as *non-radiating edges.*

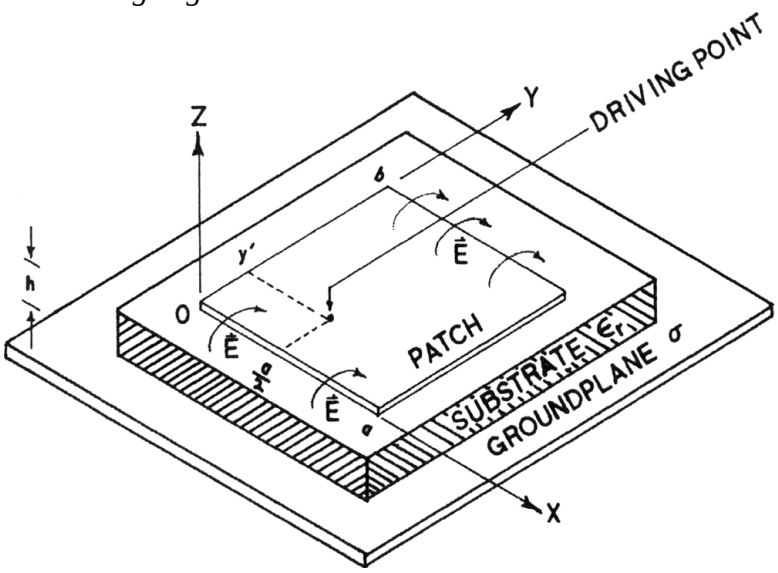

Figure 3.2

Figure 3.2 Geometry of a RMSPA

Methods of Analysis

There are many methods of analysis for microstrip antennas, which can be divided into three categories:

- **Line-transmission model**: it is the easiest of all, it gives good physical insight but is less accurate and it is more difficult to model coupling.
- **Cavity model**: it is more accurate but also more complex. However, it also gives good physical insight and is rather difficult to model coupling.
- **Full-wave models**: these are very accurate, very versatile, and can teat single elements, finite and infinite arrays, stacked elements, arbitrary shaped elements and coupling and thus they are the most popular and practical. However, they are the most complex models and usually give less physical insight.

3.1.1 Transmission-line model

The rectangular patch microstrip antenna (RMSPA) has a physical structure derived from a microstrip transmission line. Therefore, the transmission line model is the first and obvious choice for the analysis and design of a rectangular patch. In this model, the MSPA is modeled as a length of transmission line of characteristic impedance Z_0 and propagation constant $\gamma = \alpha + j\beta$. The fields vary along the length of the patch, which is usually a half-wavelength, and remain constant across the width. Radiation occurs mainly from the fringing fields at the open ends. The effect of radiation is accounted for by the radiation admittance called self-admittance Y, attached at the open ends of the transmission line.

TL model of a RMSPA

Consider a rectangular patch of dimensions $L\,x\,W$ as shown in figure. The periphery of this patch is described by four edges at $x = 0, L$ and $y = 0, W$. The four edges are classified as radiating or non-radiating depending on the field variation along their length. The radiating edge shows a slow field variation along its length, while the non-radiating edge should have an integral multiple of half-wave variations along the edge, so that there is an almost complete cancellation of the radiated power from the edge.

Should we consider the TM_{10} mode in the patch, the edges at $x = 0, L$ are radiating types because the electric field is uniform along these, while the walls at $y = 0, W$ are non-radiating types because of half-wave variation of the field along these edges. The radiating edges are characterized by load admittances $Y_s = G_s + jB_s$, where G_s is the conductance associated with the power radiated from the edge or wall, and B_s is the susceptance due to the energy stored in the fringing field near the edge. Therefore:

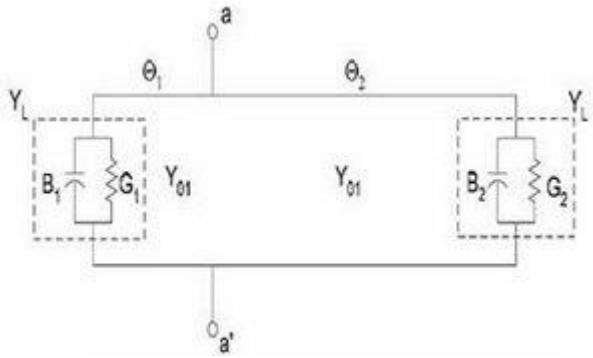

Figure 3.3

Figure 3.3 TL model of a RMSPA

Fringing Fields

It should be considered that because of dimensions of the patch are finite along the length and width, the fields at the edges of the patch undergo fringing, i.e. the field exists outside the dielectric thus causing a change in the effective dielectric constant. It is a function of the ratio of the dimensions of the patch and the height of the substrate. A typical microstrip line is a non-homogeneous line of two dielectrics (substrate and air). Most of the electric field lines reside in the substrate but parts of some lines exist in air. Fringing in this case makes the microstrip line look wider electrically compared to its physical dimensions. Since some of the waves travel in the substrate and some in air, an **effective dielectric constant** ε_{ref} is introduced to account for fringing and the wave propagation in the air.

Effective dielectric constant and length

This effective dielectric constant is defined as the dielectric constant of the uniform dielectric material so that the line inserted in this dielectric behaves the same way as it does in the actual microstrip line with two dielectrics. Therefore, the microstrip line behaves more like a homogeneous line of one dielectric (only the substrate), and the effective dielectric constant approaches the value of the dielectric constant of the substrate.

$$\varepsilon_{ref} = \frac{\varepsilon_r+1}{2} + \frac{\varepsilon_r-1}{2}\left(1 + 12\frac{h}{W}\right)^{-\frac{1}{2}}$$

Equation 3.1

Because of the fringing effects, the patch of the microstrip antenna looks electrically greater than its physical dimensions. The extension width can be computed as follows:

$$\frac{\Delta L}{h} = 0.412\frac{\left(\varepsilon_{ref} + 0.300\right)(W/h\ + 0.264)}{\left(\varepsilon_{ref} - 0.258\right)(W/h\ + 0.8)}$$

Equation 3.2

Therefore, the effective length is:

$$L_{ef} = L + 2\Delta L$$

Equation 3.3

Resonant Frequency

The resonant frequency and associated modes will be analyzed in the next section, but we can already assert that for the dominant TM_{010} mode, the resonant frequency of the microstrip antenna is a function of its length. It is usually given by,

$$f_r = \frac{c}{2L_{ef}\sqrt{\varepsilon_{ef}}}$$

Equation 3.4

By using this model, we can derive other characteristic, such as the parallel equivalent admittance for the slots or the resonant input impedance.

3.1.2 Cavity model

Microstrip antennas resemble dielectric loaded cavities, and they exhibit higher order resonances. The normalized fields within the dielectric substrate can be found more accurately by treating that region as a cavity bounded by electric conductors (above and below it) and by magnetic walls (to simulate an open circuit) along the perimeter of the patch.

Physics of the Cavity Model

Let us attempt to present a physical interpretation into the formation of the fields within the cavity and radiation through its side walls. When the microstrip patch is energized, a charge distribution is established on the upper and lower surfaces of the patch, as well as on the surface of the ground plane, as shown in Figure 3.4. The charge distribution is then controlled by two mechanisms: an attractive and a repulsive mechanism. The *attractive mechanism* is between the corresponding opposite charges on the bottom side of the patch and the ground plane, which tends to maintain the charge concentration on the bottom of the patch. The *repulsive mechanism* is between like charged on the bottom surface of the patch,

which tends to push some charges from the bottom of the patch, around its edges, to its top surface.

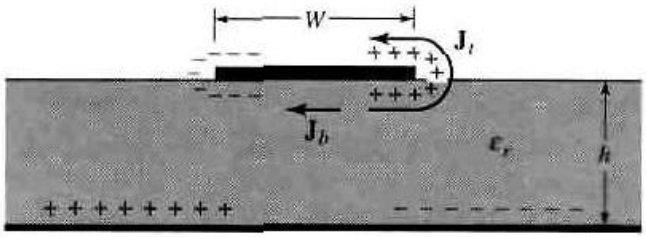

Figure 3.4

Figure 3.4. Charge distribution and current density creation on microstrip

The movement of these charges creates corresponding current densities J_b and J_r, at the bottom an top surfaces of the patch, respectively. Since the height-to-width ratio is very small, the attractive mechanism dominates and most of the charge concentration and current flow remain underneath the patch. A small amount of current flows around the edges of the patch to its top surface. However, this current flow decreases as the height-to-width ratio decreases. In the limit, this would allow the four side walls to be modeled by perfect magnetic conducting surfaces which ideally would not disturb the magnetic or electric field distributions.

If the microstrip antenna were treated only as a cavity, it would not be sufficient to find the absolute amplitudes of the electric and magnetic fields. In fact, by treating the walls of the cavity and the material within it as lossless, the cavity would not radiate and its input impedance would be purely reactive. Also, the function representing the impedance would only have real poles. To account for radiation, a loss mechanism has to be introduced: the radiation and loss resistance, which are taken into account by the effective loss tangent.

TM modes in rectangular MSPA

Because of the thickness of the microstrip is usually very small, the waves generated within the dielectric substrate undergo considerable reflections when they arrive at the edge of the patch. Thus only a small fraction of the incident energy is radiating (a very inefficient antenna). The fields beneath the patch form standing waves that can be represented by sinusoidal wave functions. Since the height of the substrate is very small compared to the wavelength within the dielectric, the field variations along the height will be considered constant. In addition, because of the very small substrate height, the fringing of the fields along the edges of the patch are also very small whereby the electric field is nearly normal to the surface of the patch. Therefore, only TM field configurations will be considered (no magnetic field in the direction of propagation).

Due to all this considerations, the volume beneath the patch can be treated as a rectangular cavity loaded with a dielectric material truncated and not extended beyond the edges of the patch.

A complete analysis implies the resolution of the vector potential that satisfies the homogeneous wave equation in order to find the electric and magnetic fields subject to the boundary conditions.

Therefore, the wave numbers k_x, k_y and k_z are obtained and are subject to the constraint equation,

$$k_x^2 + k_y^2 + k_z^2 = \left(\frac{m\pi}{h}\right)^2 + \left(\frac{n\pi}{L}\right)^2 + \left(\frac{p\pi}{W}\right)^2 = k_r^2 = \omega_r^2 \mu\varepsilon \quad \text{Equation 3.5}$$

The resonant frequencies for the cavity are thus given by

$$f_{r_{mnp}} = \frac{1}{2\pi\sqrt{\mu\varepsilon}} \sqrt{\left(\frac{m\pi}{h}\right)^2 + \left(\frac{n\pi}{L}\right)^2 + \left(\frac{p\pi}{W}\right)^2} \quad \text{Equation 3.6}$$

To determine the dominant mode, we need to examine the resonant frequencies. For all microstrip antennas $h \ll L$ and $h \ll W$. Then, if $L > W$, the mode with the lowest frequency (dominant mode) is the TM_{010} whose resonant frequency is given by

$$f_{r_{010}} = \frac{1}{2L\sqrt{\mu\varepsilon}} = \frac{v_0}{2L\sqrt{\varepsilon_r}} \quad \text{Equation 3.7}$$

In addition, the next higher order resonant mode is

$$f_{r_{010}} = \frac{1}{2W\sqrt{\mu\varepsilon}} = \frac{v_0}{2W\sqrt{\varepsilon_r}}, L > W > \frac{L}{2} \rightarrow \text{mode } TM_{010} \quad \text{Equation 3.8}$$

$$f_{r_{020}} = \frac{1}{L\sqrt{\mu\varepsilon}} = \frac{v_0}{L\sqrt{\varepsilon_r}}, W < \frac{L}{2} \rightarrow \text{mode } TM_{020} \quad \text{Equation 3.9}$$

If, however, $W > L$, the dominant mode is the TM_{010} whose resonant frequency is given by Equation 3.8 while if $L < W/2$, the second order mode is the TM_{020}. The distribution of the tangential electric field along the side walls of the cavity for the TM_{010}, TM_{001}, TM_{020} and TM_{002} is shown in Figure 3.5.

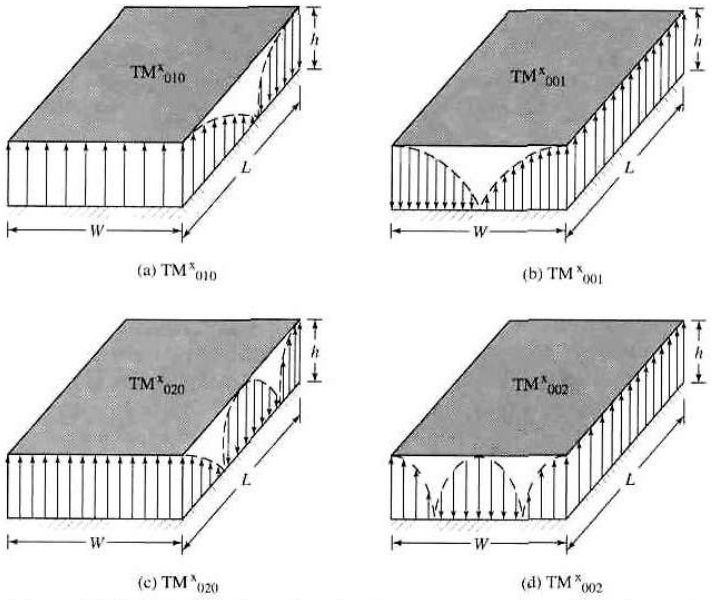

Figure 3.5

Figure 3.5 Modes for rectangular microstrip patch

By using this approach, we can also obtain other parameters, i.e., the equivalent current densities, directivity, fields radiated, quality factor of the resonator…

3.1.3 Full-wave models

The approximate models of MSPA above-described models make a number of simplifying assumptions that limit their validity:

- The models are accurate for thin substrates ($h/\lambda_0 < 0.01$) only because of the assumption $\partial/\partial z = 0$.
- These models are not accurate when applied to narrow width microstrip dipoles.
- Some of the feed configurations such as proximity-coupled and aperture-coupled microstrip feeds are difficult to model.
- Cross-polarized radiation from a patch antenna has not been predicted using the transmission line model or the multiport network mode because only a single-mode analysis has been carried out.

Types of Full-wave Models

Most of the limitations listed here can be overcome in the full-wave techniques, which maintain rigor and accuracy at the expense of numerical simplicity. The three most popular full-wave techniques are called the *spectral-domain full-wave solution,* the *mixed-potential electric field integral equation approach,* and the *finite-difference time-domain* technique. Their principal assumption of the integral equation is that the substrate and ground plane are infinite in lateral dimensions. The formulation of the solution is based on rigorously enforcing the boundary conditions at the air-dielectric interface by using the exact Green's function for the composite dielectric.

In the first approach, the integral equation is written and solved in the spectral approach. In the other approach, the spectral domain is used for calculating the Green's function, but inverse transforms are taken at this stage and the integral equation is solved in the space domain.

3.1.4 Design considerations

The effective design and analysis of microstrip antennas presupposes the quantitative knowledge of the effects of the physical and mechanical properties of the patch, the ground plane, and the substrate material on electromagnetic properties of the antenna.

A microstrip patch antenna may be of any geometrical shape and any dimension. In practice, the rectangle is a very common shape. The selection of a particular patch shape depends on the parameters one wishes to optimize: antenna size, bandwidth, efficiency, radiation pattern, side-lobes, polarization, and gain.

Substrate properties

Substrate properties. The consistency of any substrate is of critical importance: its permittivity ε_r and its thickness h determine the dimensions and operational properties of the MSPA. For example, a thick substrate of low permittivity results in a wider bandwidth

and lower efficiency than a thin substrate of high permittivity. A high permittivity reduces the patch size and the extent of the fringing fields. Consequently, the radiation is due to a narrow magnetic current ring around the patch periphery. A thicker substrate, on the other hand, does not reduce the patch size significantly, but extends the zone of the fringing fields, thus resulting in a broad a radiation ring. The most popular substrate materials are honeycomb ($\varepsilon_r = 1.07$), Duroid ($\varepsilon_r = 2.32$), quartz ($\varepsilon_r = 3.8$), FR-4 ($\varepsilon_r = 4.4$) and aluminia ($\varepsilon_r = 10$).

Antenna losses

Antenna losses. We can identify three types of losses in MSPA. In the first place, the existence of a dielectric substrate over a conducting ground plane can cause the excitation of **surface waves** along the air-dielectric interface and within the substrate. These surface waves propagate parallel to the interface without attenuation and **radiate** some of their energy as the reach the microstrip discontinuity. A grounded dielectric layer always supports a finite number of surface wave modes, but since the lowest order TM-type mode has a zero cutoff frequency, a MSPA will, in general, always excite some surface-wave power. Except for very thin substrates, **conductor** and **dielectric losses** are quite small. The dielectric loss displays strong dependence on frequency and is independent of surface roughness, and can be minimized by choosing a low-loss substrate. The conductor losses, however, depend on frequency and substrate surface roughness, and are more difficult to control.

Dimensions

Dimensions. The proper selection of patch dimensions of a rectangular MSPA is important in the design, because the antenna performance characteristics depend firmly on the physical dimensions. RMSPA radiates efficiently when it resonates, which means that the patch length is approximately one-half of the wavelength in the substrate medium. However, the fringing capacitance effect should always be considered. Besides, the patch length affects the resonant resistance and the E-plane radiation pattern. The patch width affects the resonant frequency, the efficiency, the bandwidth, the H-plane radiation pattern, and the cross polarization. To select the patch width properly, it must be considered that, due to the excitation of surface waves, a small width result in a large bandwidth, and low antenna efficiency and gain. However, a large width results in the excitation of higher order modes, which may distort the radiation pattern, decrease the bandwidth, and increase the efficiency.

In the literature, we can find several CAD formulas for the dimensions. Kara [23-25] has carried out a number of experimental investigations on the resonant frequency for the TM_{10} mode of a RMSPA. The length was calculated as seen before, which fits the measured resonant frequency of practical antennas within 1.6%. The value of the patch width *W*, necessary to obtain 50Ω input impedance, was found to be given by

$$W = \sqrt{h\lambda_d}[\ln(\lambda_d/h) - 1\,] \qquad \text{Equation 3.10}$$

Guney [27] analyzed the dependence of the patch length and width on antenna parameters. A model for the patch length and width expressions is chosen first, then the unknown coefficient values of the model are obtained by using a curve-fitting technique (CFT). The theoretical patch length and width results obtained using the expressions derived in his study agree well with the measured results:

$$L = \begin{cases} 0.51\lambda_d(h/\lambda_d)^{0.0112} - 0.565h(h/\lambda_d)^{-0.117} + 0.014\lambda_d, & \text{if } h/\lambda_d \leq 0.13 \\ 383.0445\lambda_d(h/\lambda_d)^{0.00052} + 0.36h(h/\lambda_d)^{0.014} - 239.37\lambda_d, & \text{if } h/\lambda_d > 0.13 \end{cases} \quad \text{Equation 3.11}$$

$$W = \begin{cases} 9.8636\lambda_d(h/\lambda_d)^{0.4561} - 10.9h(h/\lambda_d)^{-0.446} + 0.00204\lambda_d, & \text{if } h/\lambda_d \leq 0.13 \\ 383.466\lambda_d(h/\lambda_d)^{-0.000907} - 0.0003h(h/\lambda_d)^{-0.04} - 239.73\lambda_d, & \text{if } h/\lambda_d > 0.13 \end{cases} \quad \text{Equation 3.12}$$

Furthermore, in Ali Akdagli 's work [28-29] the formulas are developed by utilizing a differential evolution, which is a simple, fast, and robust evolutionary algorithm that has proven effective in determining the global optimum for general type of numeric optimization. His formulas provide < 0.16% and 0.22% error on average for the patch length and patch width, respectively:

$$L = \begin{cases} 0.483\lambda_d - 0.5957h + 0.0281\lambda_0 \cos((h/\lambda_d)^{-0.02142}), & \text{if } h/\lambda_d \leq 0.13 \\ 0.265\lambda_d + 1.4097h + 0.0029\lambda_0 \cos((h/\lambda_d)^{-1.099}),, & \text{if } h/\lambda_d > 0.13 \end{cases} \quad \text{Equation 3.13}$$

$$W = \begin{cases} 0.5913\lambda_d - 2h + 0.3211\lambda_0 \cos((h/\lambda_d)^{-0.1798}), & \text{if } h/\lambda_d \leq 0.13 \\ 1.2848\lambda_d - 3.636h + 0.4469\lambda_0 \cos((h/\lambda_d)^{-0.5626}),, & \text{if } h/\lambda_d > 0.13 \end{cases} \quad \text{Equation 3.14}$$

The Feed. Power can be coupled into or out of the antenna element by two primary methods, namely, the direct contact and the electromagnetic induction. The first method uses a transmission line contact either by a microstrip line or by a coaxial probe from underneath the substrate. In the electromagnetic induction or the noncontact method, there is no direct physical or electrical contact between the patch and the feeding structure, and the coupling to the antenna element is made strictly by electromagnetic induction, either directly from the feeding microstrip or through an intermediate aperture.

Coaxial Feed

The coaxial feed, also called the probe feed, can be used to feed patch elements through the ground plane from a parallel feed substrate. Its location is usually selected to provide a perfect match between the antenna and the transmission line. The resonant resistance increases as the feed moves away from the center of the patch. The variation of input resistance at resonance with feed position essentially follows that of the cavity field. For the lowest mode, it is usually large when the feed is near the edge of the patch, and decreases as the feed moves inside the patch. The 50Ω- input resistance point may be obtained by varying the distance from the radiating edge of the antenna element to the feed location, as shown in

Equation 3.15

Equation 3.15. The input impedance at the center of a patch is zero because the voltage is zero and the current is a maximum. If the feed is located at x_{feed} and $0 \leq y_{feed} \leq W$, the input resistance at resonance for the dominant TM_{10} mode can be expressed as

$$R_{in} = R_r \cos^2(\pi x_f / L), \qquad R_r \geq R_{in}$$

Microstrip Line Feed

For the case of a microstrip line feed, the patch can be notched to provide an inset feed point. Such direct conducting feeding methods have the advantage of simplicity, but also have several disadvantages. These configurations suffer from the bandwidth feed radiation tradeoff, where an increase in substrate thickness for the purpose increasing of bandwidth leads to an increase in spurious feed radiation, increased surface wave power, and possibly increased feed inductance.

In Basilio's work [26], the impedance was measured for the inset microstrip fed patches. As with the probe-fed case, the maximum input resistance occurs at the edge of the patch and decreases as the inset distance is increased toward the center of the radiator, while the reactance remains reasonably constant. However, the rate at which the resistance decreases with changing feed position is seen to be much more rapid, and the resistance is also seen to rise slightly as the inset approaches the center of the patch. The latter behavior is in contrast to the probe-fed case, where the resistance became essentially zero near the center. Empirically, a $\cos^4(\pi x_f / L)$ would seem to be the best fit for the experimental data, but there is no real theoretical justification.

Ground Plane, Input Impedance and Bandwitdth

Ground Plane. Microstrip antennas are shielded by a ground plane which limits the radiation to a half plane and combined with an effective two-slot radiation from adjacent edges. Its size controls the back radiation, and also affects the excitation efficiency of non-resonant modes. The thickness of the ground plane affects the reflection coefficients of various modes, at its terminal edge, and also their excitation efficiency.

Input Impedance. The input impedance of an antenna directly affects the efficiency of energy transfer to or from the antenna. It varies according to the antenna properties such as the excitation frequency, the permittivity and thickness of the substrate, patch length and width, and the location of the feed point. Owing to its effects on the efficiency of energy transfer, it should be determined accurately in order to provide a good match between the patch and the feed.

Due to the resonant nature of the investigated antenna element, its resonant input resistance is related to the quality factors associated with the system losses. A properly chosen patch shape may result in an impedance versus frequency behavior that approximates a parallel RLC circuit. The operating frequency is determined when the impedance becomes purely real.

Bandwidth. Since the cavity under the patch is basically a resonator, the total quality factor Q and the impedance bandwidth are dependent on the thickness of the substrate and its permittivity. This implies that the quality factor of a patch antenna on a thin substrate is

large, and that the bandwidth is small. Bandwidth improves as the substrate thickness is increased, or as the permittivity of the substrate is reduced.

Radiation Patterns, Efficiency and Polarization

Radiation Patterns. Radiation from a rectangular microstrip antenna operating in the TM_{10} mode occurs mainly from the fringing fields between the edge of the patch conductor and the ground plane. These fields can be resolved into normal and tangential components with respect to the ground plane. The tangential components (those parallel to the ground plane) are in phase, and are combined to give a maximum radiated field normal to the ground plane. The patch is linearly polarized with the electrical field lying in the same direction as the patch length. The E-plane is the plane perpendicular to the radiating edges, and lies along the patch length. This plane widens mainly with increasing permittivity but it is not affected by patch width. Furthermore, for angles very near the horizon, the pattern depends strongly on the truncation of the dielectric substrate. Because the patterns are broad, they can also be affected by finite size ground planes, ridges, and bumps. For very small ground planes, ripples can be introduced into the pattern over a wide range of angles, and also some of the radiation can spill over onto the backside of the ground plane. However, by using an appropriate size of the ground plane, the ripples in the main pattern can be diminished. Note that the half-power beamwidth in the E-plane decreases with increasing substrate thickness. The beamwidth can also be increased by choosing a small patch size.

The H-plane lies parallel to the patch width, and its beamwidth is a function of patch width. The H-plane patterns are independent of the substrate permittivity.

Efficiency. The efficiency of an antenna depends on the shape and size of the patch and on the electric size of the patch and on the electric size and consistency of the dielectric substrate. Antennas printed on high-permittivity dielectric materials exhibit a low efficiency due to the excitation of surface waves.

Polarization. Normally, conventional rectangular MSPA are linearly polarized radiating structures. But they can be designed to radiate with two orthogonal linear polarizations or with circular polarization.

3.1.5 Probe-Fed Microstrip Rectangular Patch Antenna for 2.4 GHz

Antenna Design

A probe-fed microstrip rectangular patch antenna functioning at 2.4 GHz is design with HFSS software, printed on a FR4 board and its performance is tested and discussed in comparison with the software simulation.

Using the above-presented equations, we have designed the patch antenna with $W = 25.6$ mm (Equations 2.10-14) and $L = 29.7$ mm.

It has been shown that similar results for finite and infinite ground plane can be obtained if the size of the ground plane is greater than the patch dimensions by approximately six times the substrate thickness all around the periphery.

Hence, for this design, the ground plane dimensions would be given in Equations 16 and 17:

$$L_g = 6h + L = 39.4\ \text{mm} \quad \text{Equation 3.16}$$

$$W_g = 6h + W = 35.2\ \text{mm} \quad \text{Equation 3.17}$$

A coaxial probe type feed is to be used in this design. As shown in Figure 4.1, the center of the patch is taken as the origin and the feed point location is given by the co-ordinates (W_f, L_f) from the origin. The feed point must be located at that point on the patch, where the input impedance is 50 ohms for the resonant frequency. Although the feed point can be selected anywhere along the patch width, it is better to choose $W_f = W/2$ so that other modes are not excited along with the TM_{10} mode. Determination of the exact feed point requires an iterative solution but it has been suggested [6-8] an approximation as shown in Equation 18:

$$L_f = \frac{L}{2\sqrt{\varepsilon_{ref(L)}}} \quad \text{Equation 3.18}$$

where $\varepsilon_{ref(L)}$ is obtained the same way as in Equation 3.1 but substituting L for W.

Therefore, the point search is $L_{ef} = 7.4\ \text{mm};\ W_f = 12.8\ \text{mm}$.

Results

For this configuration we have obtained a center frequency of 2.55 GHz. By increasing the patch width W until 28.12 mm we have reached the 2.4 GHz. Broader bandwidth (2.37-2.43 GHz) and impedance approximately 50-60Ω have been achieved by tuning the patch length to 30.4 mm. The simulation shows the following:

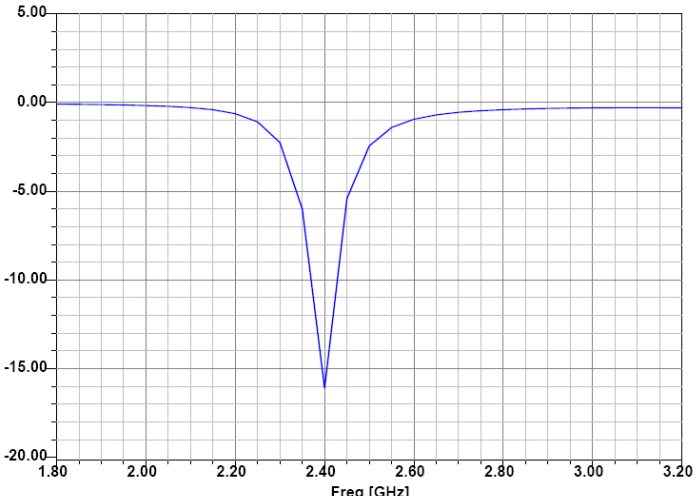

Figure 3.6. Return Loss

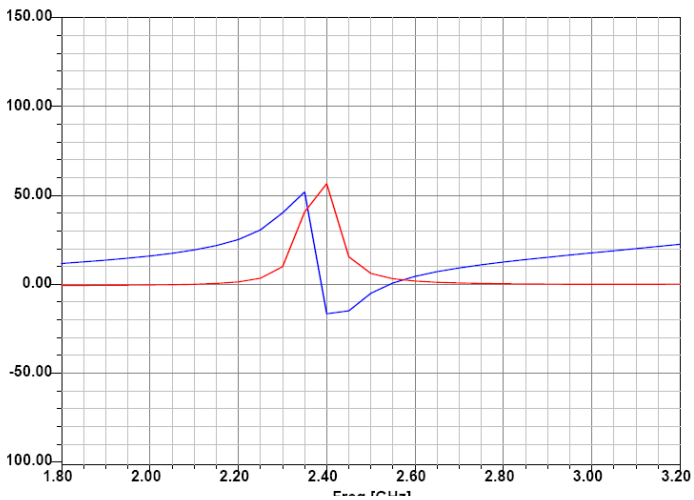

Figure 3.7. Real and Imaginary Impedance

The last modification introduced has been increasing the ground in order to achieve a better return loss (14 mm have been added to both ground width and length in order to obtain -29 dB return loss).

Once the patch antenna has been fabricated, a network analyzer has been used to measure the antenna return loss characteristic. We have can see a shift in the frequency of the fabricated antenna in comparison with the simulation (see Figure 3.8).

Most fabrication errors arise because of inaccuracy in etching; etching accuracy depends on the process and the materials used in the photo-etching process, the substrate surface finish, and metallization thickness. Because of fabrication errors, tolerances and other effects, the electromagnetic characteristics of a microstrip antenna may deviate from the design specifications. Dimensional tolerances and substrate inhomogeneitites can result in amplitude and phase errors, and also in variation in the resonant frequency of the antenna.

Errors, Corrections and Final Results

Deviations in effective electrical dimensions caused by slight variations in finished antenna length, variations in the relative permittivity of the substrate material, or non-uniformity in the substrate thickness can lead to discrepancies between the designed and actual resonant frequencies.

The data obtained from the network analyzer settles the center frequency in 2.459 GHz with a return loss of -30.47 dB. Since an increase in the patch length causes a decrease in the resonant frequency we have added an extra copper strip in the patch to increase the length (Figure 3.10). The final return loss results are shown in Figure 3.11.

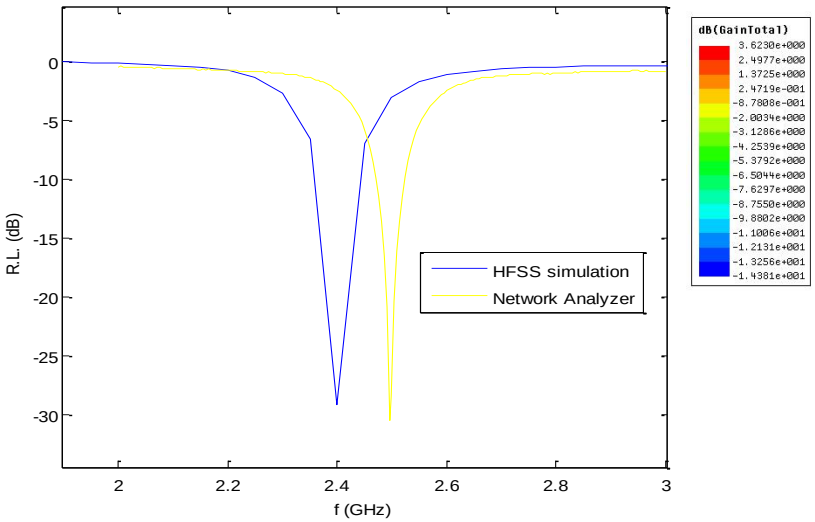

Figure 3.8 Return Loss Comparison

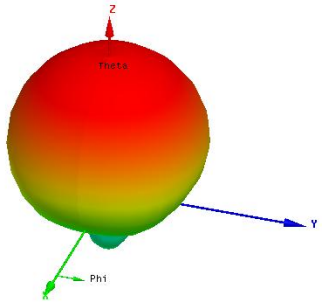

Figure 3.9 HFSS Antenna Gain

Figure 3.10 Final Antenna

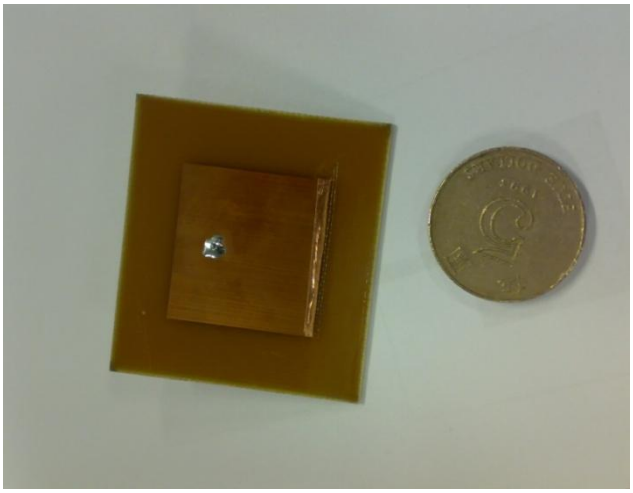

Figure 3.11 Return Loss Comparison

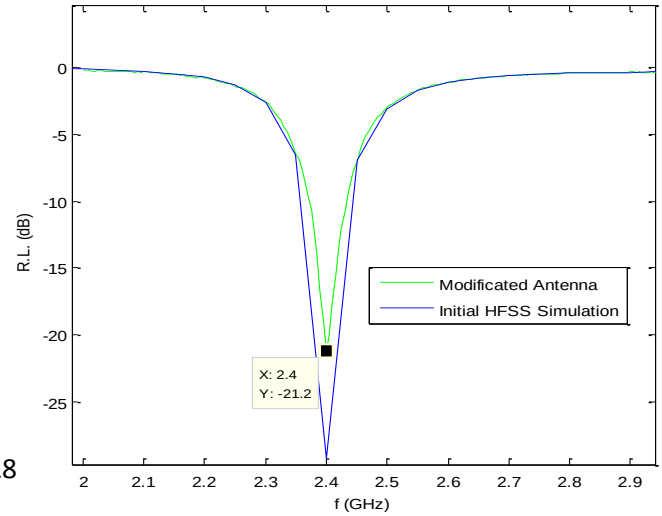

3.2 Triangular Microstrip Patch Antennas

The triangular geometry of the microstrip patch (TMP) drew the attention of the researchers in investigating the structure as planar circuit components and as radiating elements in conventional and multilayered configurations [30]. Compared to other patch geometries, the triangular microstrip is physically smaller having radiation properties similar to the rectangular patch but has a lower radiation loss [31]. In recent years, the TMP has found several new applications as broadband radiators, dual frequency and multiband antennas, circularly polarized antennas and in designing arrays. Several new modified configurations due to its easy conformability have also been reported in literature [30].

Promising use of the triangular patch as array is recently reported in [32]. It is used for the Engineering Test Satellite VIII (ETS-VIII) launched by Japan Aerospace Exploration Agency to support the next generation of mobile satellite communications. The antenna comprises of three equilateral triangular patches operating at 2.50 and other 3 patches at 2.65 GHz having 5 dBi gain. This is not the only design carried out using arrays of triangular patches, since the conformal shape and geometry makes this patch an attractive element to be used for array designs.

Field Distribution and Resonant Frequencies

The field distribution in a triangular patch can be found using the cavity model, in which the triangle is surrounded by a magnetic wall along the periphery as was done for the rectangular configuration.

Consider a triangular resonator with magnetic side walls filled with a dielectric material of relative permittivity ε_r and thickness h. Since $h \ll \lambda_0$ there is no variation of the fields along the z direction (normal direction to the patch surface), therefore, the structure supports TM modes.

The resonant frequency corresponding to the various modes is:

$$f_{m,n,l} = \frac{2c}{3a\sqrt{\varepsilon_r}}\sqrt{m^2 + mn + n^2} \qquad \text{Equation 3.19}$$

where m,n,l cannot be zero at the same time and satisfy the condition that $m + n + l = 0$, c is the velocity of light in the free space, and a is the side length of the equilateral triangle.

The above expression is valid when the triangular resonator is surrounded by a perfect magnetic wall. The effect of a non-perfect wall on the resonant frequency has been widely discussed. Most of the suggestions are about replacing the side length a by an effective value a_e and leaving the substrate dielectric constant unchanged. The other set of suggestions proposes replacing both a and ε_r with their effective values. An expression for a_e has been arrived at by curve fitting the experimental and theoretical results for the resonant frequency for TM_{10} mode, which corresponds to the dominant mode [33]. It is given by

$$f_{1,0,-1} = \frac{2c}{3a_e\sqrt{\varepsilon_r}} \qquad \text{Equation 3.20}$$

Knowing f_{10} from above, the resonant frequency for higher modes is calculated as follows

$$f_{m,n,l} = \frac{2c}{3a_e\sqrt{\varepsilon_r}}\sqrt{m^2 + mn + n^2} \qquad \text{Equation 3.21}$$

Effective Side Length

Dahele and Lee [34] proposed a value for a_e that are within 2 per cent of the measured frequencies

$$a_e = a + \frac{h}{\sqrt{\varepsilon_r}} \qquad \text{Equation 3.22}$$

Chen and Lee [33] proposed a value for the effective side length that is claimed to be within 0.5% when compared with the value obtained from the moment method analysis:

$$a_e = a\left[1 + \frac{2.100h}{a} - 12.853\frac{h}{a\sqrt{\varepsilon_r}} + 16.436\frac{h}{a\varepsilon_r} + 6.182\left(\frac{h}{a}\right)^2 - 9.802\frac{1}{\sqrt{\varepsilon_r}}\left(\frac{h}{a}\right)^2\right] \qquad \text{Equation 3.23}$$

Among the solutions that propose replacing both a and ε_r with their effective values, Gang [35] suggested that the side length in a should be replaced by the same effective value given in Equation 4 but he replaced ε_r with the following effective value:

$$\varepsilon_{r,ef} = \frac{1}{2}(\varepsilon_r + 1) + \frac{1}{2}(\varepsilon_r - 1)\alpha_1 \qquad \text{Equation 3.24}$$

where

$$\alpha_1 = \frac{[\sqrt{(A+H)H} - A\ln(\sqrt{H} + \sqrt{H+A})]}{H} + \frac{A\ln(A)}{2H} \qquad \text{Equation 3.25}$$

with

$$A = 6\sqrt{3}h \qquad H = \frac{\sqrt{3}a}{2} \qquad \text{Equation 3.26}$$

Güney [36], used the last Equations 6-8 to calculate the effective side length as follows:

$$a_e = a + \frac{h^{0.6}a^{0.38}}{\sqrt{\varepsilon_{r,ef}}} \qquad \text{Equation 3.27}$$

This new effective side length has been found to be the measured and theoretical data closely [36].

By using the same cavity model, the input impedance of an equilateral triangular patch antenna has been determined using the cavity model and integral equation approach and has been seen to vary sharply with frequency, indicating a high value of resonator *Q*.

CHAPTER IV. DUAL-FREQUENCY AND BROAD-BAND TRIANGULAR MSPA

Patch antennas are popular for their well-known attractive features, such as low profile, light weight, and compatibility with monolithic microwave integrated circuits (MMICs). Their main disadvantage is an intrinsic limitation in bandwidth, which is due to the resonant nature of the patch structure.

In the design following, we place two resonant frequencies near each other in order to obtain a broadband antenna functioning at 2.4GHz with a final bandwidth of 110 MHz (4.58%). This has been achieved using a technique characteristic in dual-frequency patch antennas.

Modern communication systems, such as those for satellite links (GPS, vehicular, etc.), as well as emerging applications, such as wireless local networks (WLAN), often require antennas with compactness and low-cost, thus rendering planar technology useful, and sometimes unavoidable. From this applications, a new motivation is given for research on innovative solutions that overcome the bandwidth limitations of patch antennas, an a valid alternative to the broadening of total bandwidth is represented by dual-frequency patch antennas. Dual-frequency antennas exhibit a dual-resonant behavior in a single radiating structure [38].

There are three main approaches to design dual-frequency antennas, which will be identified as 1) *orthogonal-mode dual-frequency patch antennas,* 2) *multi-patch dual-frequency patch antennas,* and 3) *reactively-loaded dual-frequency patch antennas.*

The most popular technique for obtaining the dual-frequency behavior is to introduce a reactive loading to a single patch. A kind of reactive loading can be introduced by etching slots on the patch. This allows for a strong modification of the resonant mode of the patch, particularly when the slots are oriented to cut the current lines of the unperturbed mode.

In the designed we are concerned with, we start creating a single-feed triangular patch antenna working at around 2.40 GHz. Afterwards, we load the antenna with two pairs of narrow slots in the triangular patch, with one pair of the slots embedded close to the side edges of the patch and the other pair inserted at the bottom edge of the patch. The two operating in this case are associated to the resonant modes of TM_{10} and TM_{20}. It is found that due to the slots embedded close to the side edges, the radiation pattern of the TM_{20} mode, which usually exhibits a slight dip in the broadside direction [36-37], is removed and become similar to that of the TM_{10} mode. As for inserting the pair of slots at the bottom edge of the patch, various frequency ratios of the two operating frequencies can be obtained by varying the length and position of the inserted slots.

Moreover, it is found that by further protruding a narrow slot out of the embedded slots close to the side edges, the frequency ratio of the two frequencies can be adjusted to be close to unity, which means broad-band radiation is obtained. This broad-band operation is especially important for the triangular microstrip antenna. This is because although the

conventional triangular microstrip antenna has the advantage of physically smaller for operating at a given frequency, as compared to the rectangular or circular microstrip antennas, it also exhibits a smaller antenna bandwidth than the rectangular or circular ones.

With the present design technique, the proposed triangular microstrip antenna can have a wider operating bandwidth with a smaller antenna size as compared to the conventional rectangular or circular microstrip antennas. Details of the proposed antenna designs are described and experimental results for the obtained dual-frequency and broad-band performance are presented and discussed.

4.1 Design

The initial patch consists of a equilateral triangular patch of a=36.5 mm of side length mounted on a FR-4 substrate board of $\varepsilon_r = 4$ and $h = 1.6$ mm. According to the equations seen in last chapter**,** this should provide a resonant frequency of approximately 2.5GHz for the TM_{10} mode and around 5GHz for the TM_{20} mode.

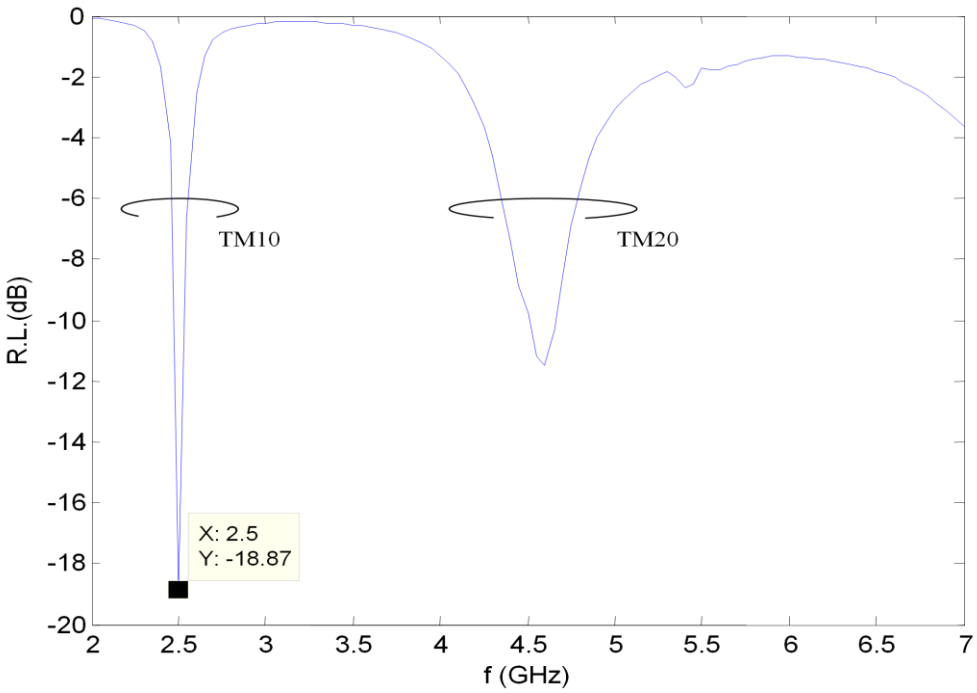

Next, the feed location d is calculated such that the input resistance of the antenna matches the characteristic impedance of the feed line. The patch is feed by a coaxial probe situated in the median of the triangle. Different feed positions are investigated for better matching. The simulations show that varying the feed position only causes a change in impedance and return loss, but not in the resonant frequencies.

First and second slots: dual-frequency design

The geometry of the dual-frequency antenna is depicted in Figures 4.1 and 4.2. The proposed design in Fig. 4.1 is denoted here as a simple slot-loaded triangular microstrip antenna and can be treated as a special case of the design in Fig. 4.2.

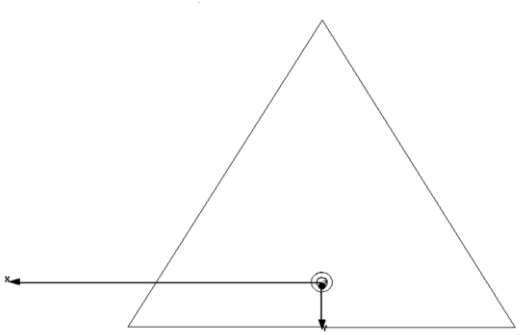

Figure 4.1 Initial Triangular Patch

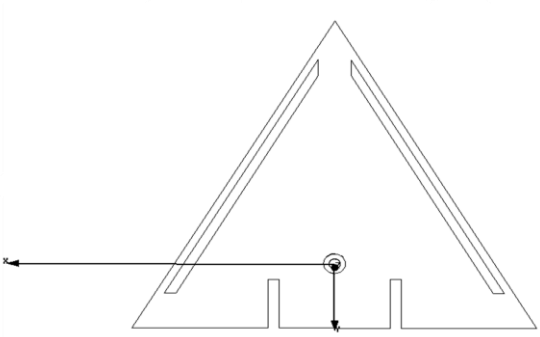

Figure 4.2 Patch with Slots 1 and 2

For both cases, the pair of slots (denoted as slot 1 in this study), having dimensions $w_1 \; x \; l_1$, are placed in parallel to the side edges of the triangular patch, with a small distance away from the side edges and separated with a distance s_1 between them. In Fig.4.2, another pair of slots (denoted as slot 2 here) with dimensions $w_2 \; x \; l_2$ are inserted at the bottom edge of the triangular patch and centered with respect to the center line of the patch with a spacing of s_2. These two pairs of slots are also of narrow width. The length of slot 1 is selected to be about 0.8 times the side length of the patch, and the distance between slot 1 and the side edge is chosen to be 1 mm approximately in this study.

Due to the presence of these slots, the fundamental resonant frequency of the triangular patch is found to be slightly affected, because slot 1 is mainly in parallel to the excited patch surface current density of the TM10 mode and slot 2 is placed near the bottom edge of the patch, where the patch surface current distribution of the TM10 mode is relatively very weak (see the related simulated results shown below).

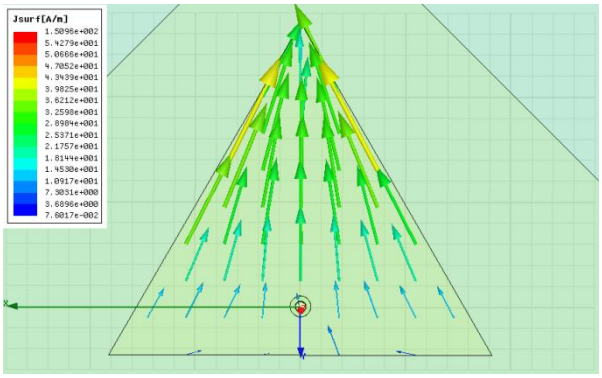

Figure 4.3 Current Distribution at the First R.F.

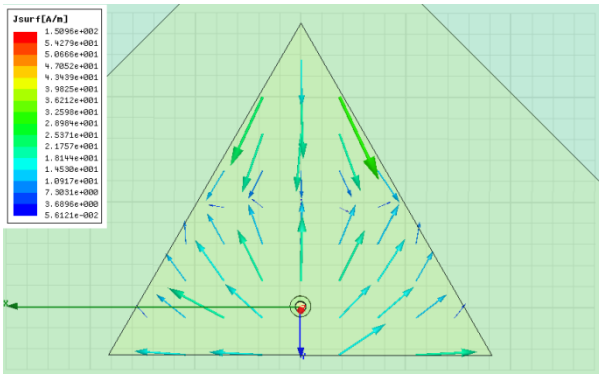

Figure 4.4 Current Distribution at the Second R.F.

The TM10 frequency first decreases with the introduction of the slot 1 with $s_1 = 0$ but it increases again as s_1 does. This had already been foreseen since the main single triangular patch has been designed initially for working at 2.5 GHz so that the decrease introduced in the first resonant frequency helps to reach the 2.4 GHz or even better, slightly less.

However, with the presence of slot 1, the surface current distribution of the TM20 mode is modified such that the small dip in the broadside direction of the radiation pattern is removed [36-37].

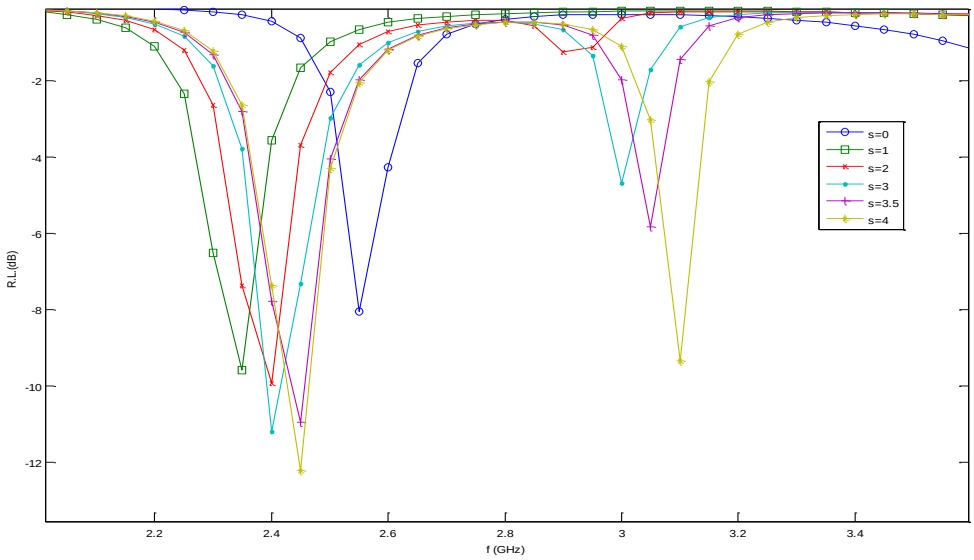

Graphic 4.1. Return Loss for Different Slot-1 Separations (s1)

Once chosen the separation between the two type-1 slots, any change in the feed position will: 1) not change the first resonant frequency but only its impedance, and 2) sometimes change slightly the second resonance (depending on the s_1 separation). This latter effect will have to be considered when we discuss the more complicated arrays of triangular antennas.

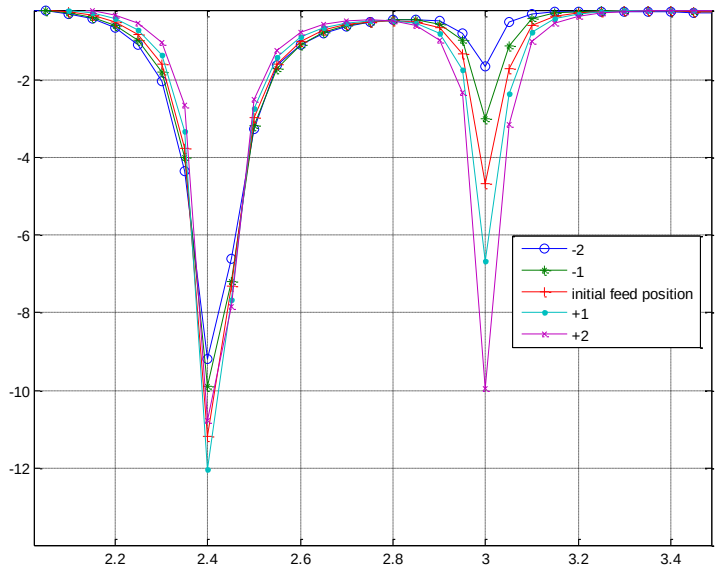

Graphic 4.2. Return Loss for Different Feed Positions

By inserting slot 2 at the bottom edge of the patch, the excited surface current paths of the TM20 modes are lengthened, which effectively lowers the resonant frequency of the TM20 mode. This suggests that by varying the positions and lengths of slot 2, the frequency ratio of the two operating frequencies can be adjusted. A single probe feed for the excitation of the TM10 and TM20 modes can also be easily located along the center line of the patch in this design.

In all the simulations, the slot-2 width has remained constant and we have changed the separation and lengths of the slots. It has been shown that as both the separation s_2 and length l_2 increase, the first resonant frequency decreases a little, but this effect can be almost neglected with some exceptions. On the other hand, this really affects the second resonant frequency, decreasing it much faster than in the latter case. As for the relation between the slot length l_2 and the separation s_2 between slots, we can assert that the bigger the s_2 is, the more quickly the decrease isof the second resonant frequency due to the increase of l_2. Some graphics are included for reference:

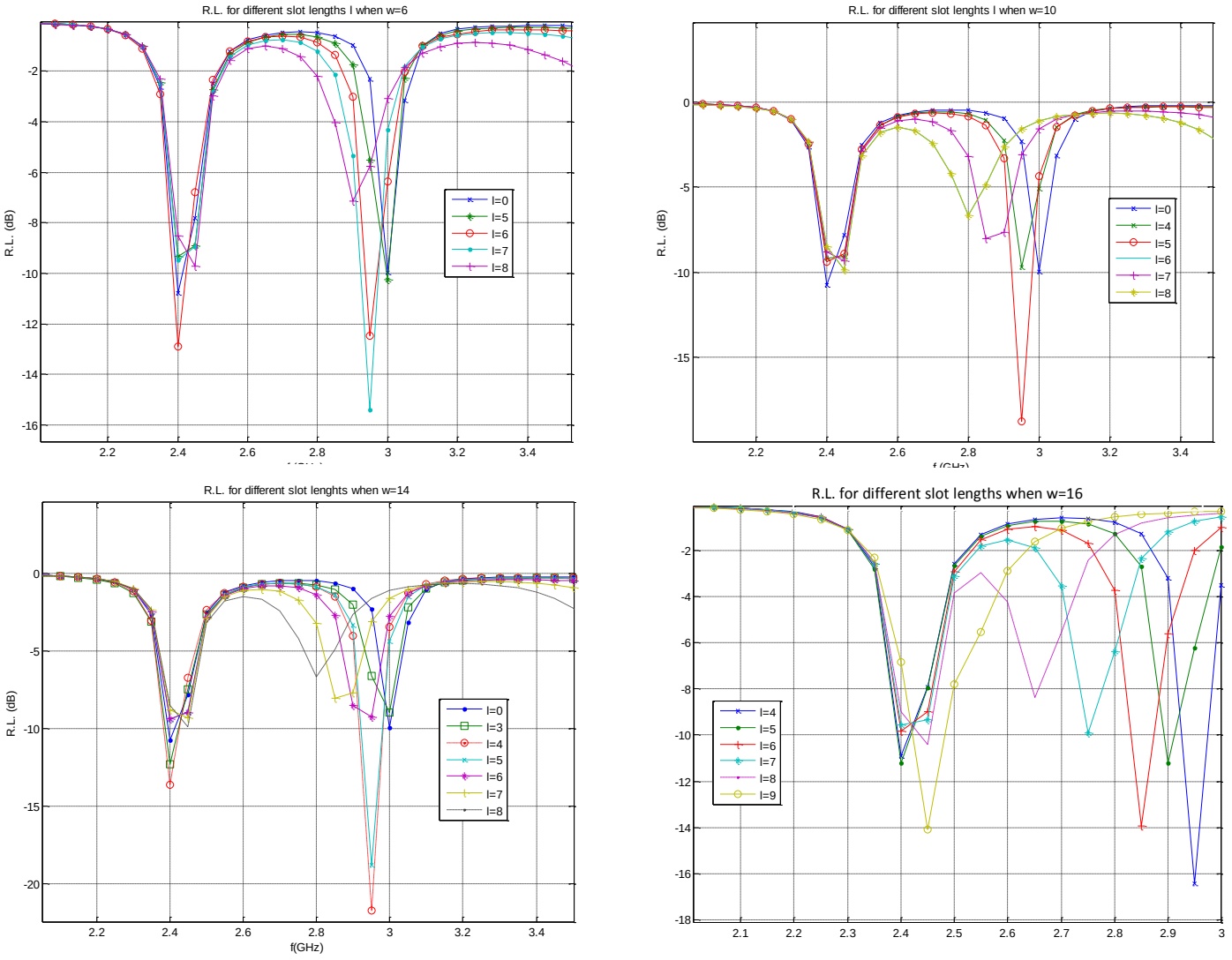

Graphic 4.3. Return Loss for Different Slot-2 Dimensions

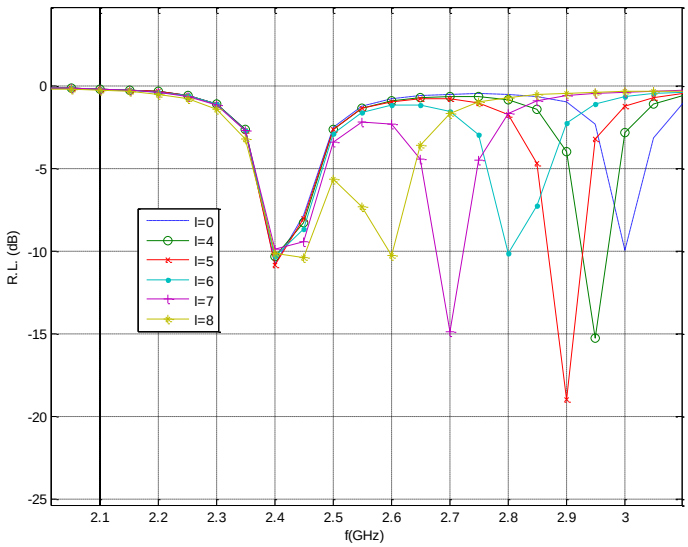

Graphic 4.4. Return Loss for Different Slot Lengths when w2=18

As we can see in the figures, dual-frequency triangular antenna can be achieved by using this technique.

Third slot: broad-band design

The next step is to make the first two broadside-radiation modes (TM10 and TM20) of the triangular patch [36-37] to be excited at frequencies close to each other to form a wider operating bandwidth. For this purpose, as referred to the antenna structure in Fig. 4.5, a pair of slots (denoted as slot 3 here) with dimensions $l_3\ x\ w$ is protruded from slot 1 at a distance d_3 away from the bottom edge of slot 1. When is selected to be less than 0.2 times the patch's side length , the perturbation of slot 3 on the fundamental resonant frequency can be greatly reduced, because in this case slot 3 will be in the region near the bottom edge of the patch where the patch surface current distribution of the TM mode is relatively very weak.

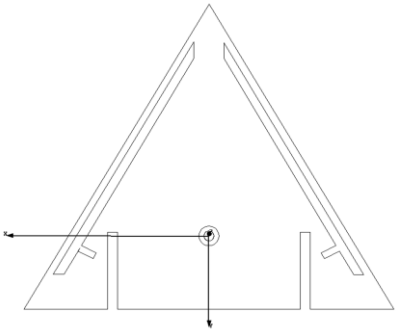

Figure 4.5 3-slotted Patch

On the other hand, it is expected that with the presence of slots 1, 2, and 3, the equivalent patch surface current path of the TM mode is strongly meandered and, thus, the resonant frequency can be significantly lowered and it occurs at a frequency close to the first resonant frequency.

After designing this antenna, we can compare the patch current distributions in the models with and without the slot 3 for the two resonant frequencies. The final results are also shown in the graphics below.

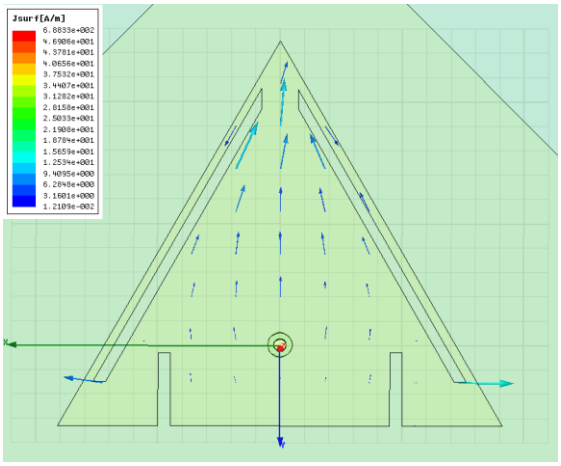

Figure 4.6 Current Distribution at the First R.F.

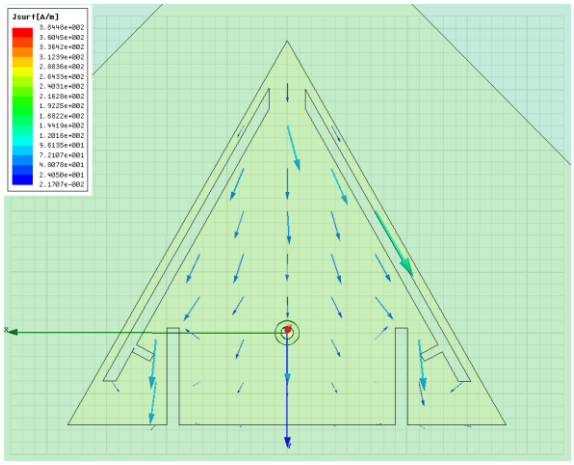

Figure 4.7 Current Distribution at the First R.F.

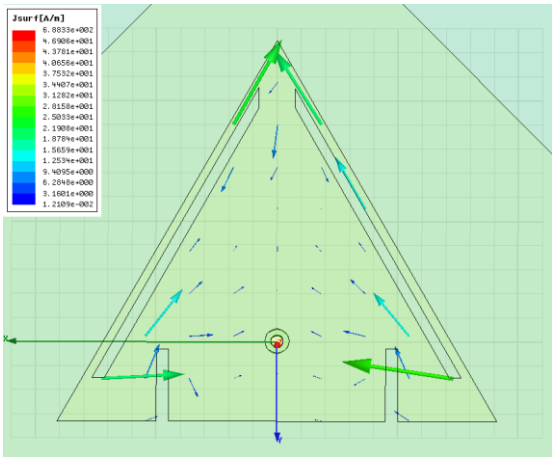

Figure 4.7 C.D. at the Second R.F. with slot 3

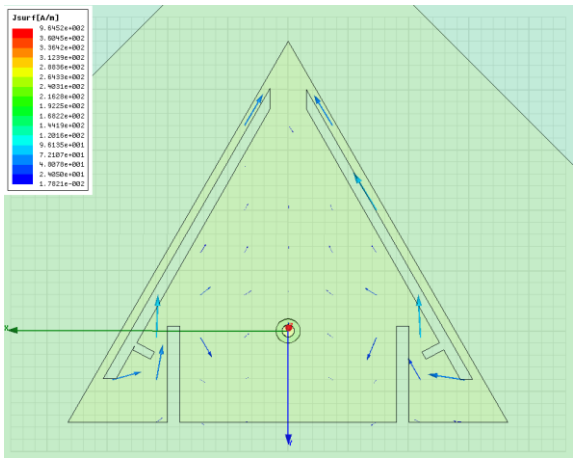

Figure 4.8 C.D. at the Second R.F. with slot 3

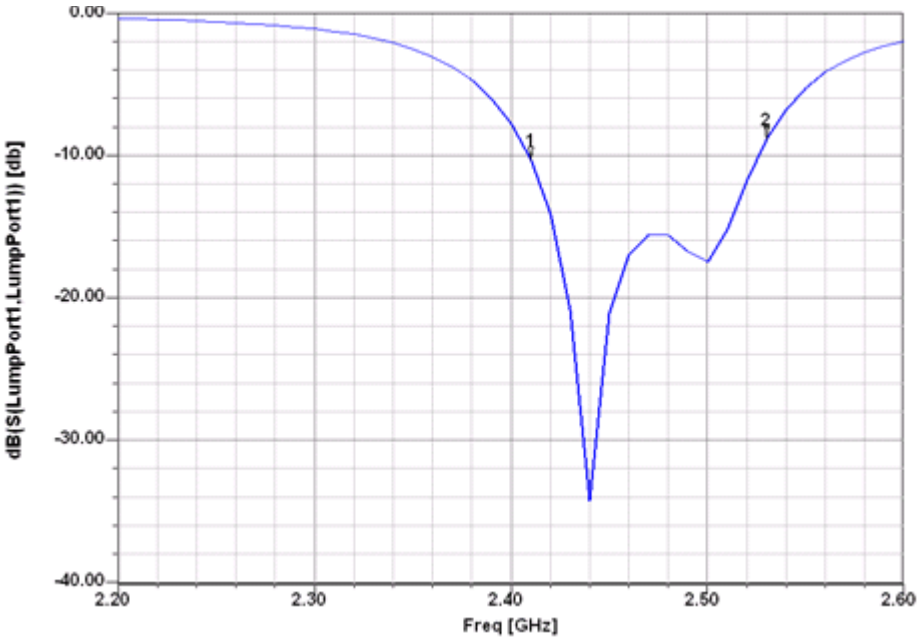

Graphic 4.5 R.L. of the three-slotted patch

As we can see in the above figure, there's been an unwanted shift in the response in frequency in the triangular antenna, in such a way that the broadband extends from 2.41 until 2.52 GHz. In the case we want to fix this without redesigning the entire antenna we will have to consider the different approaches which can be applied.

In the first place, the easiest way to decrease the first resonant frequency is to increase the patch side length. Doing this by 2 mm, we manage to decrease the first resonance frequency – which was settled in 2.44 GHz – down to 2.38 GHz while the second resonant frequency remains at around 2.52 GHz.

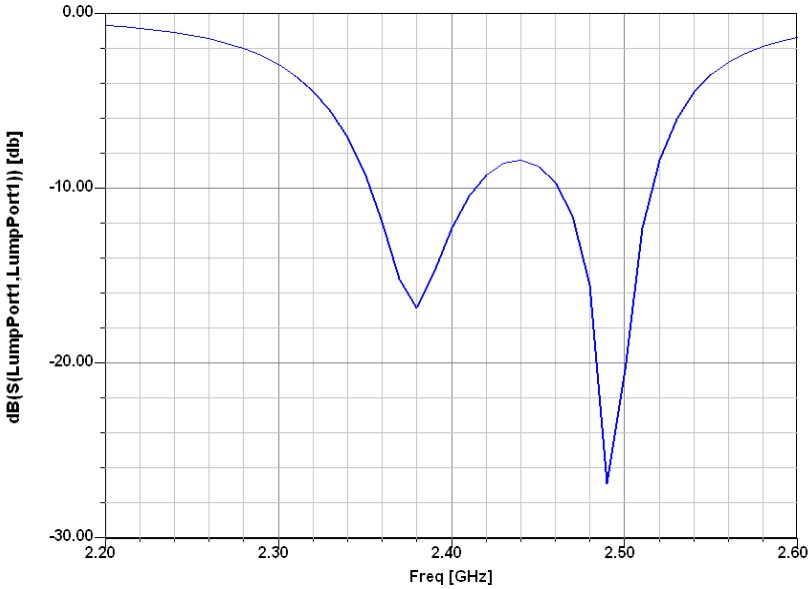

Graphic 4.6 R.L. of the modified three-slotted patch

Now, the bandwidth is 2.36 – 2.50 GHz but there is a part from 2.42-2.46 where the antenna stops resonating properly (Graphic 4.6). This is because the two resonant frequencies are too far apart from each other. In order to reduce the second resonant frequency we can change the dimension and position of slot 2. A graphic will show this effect better.

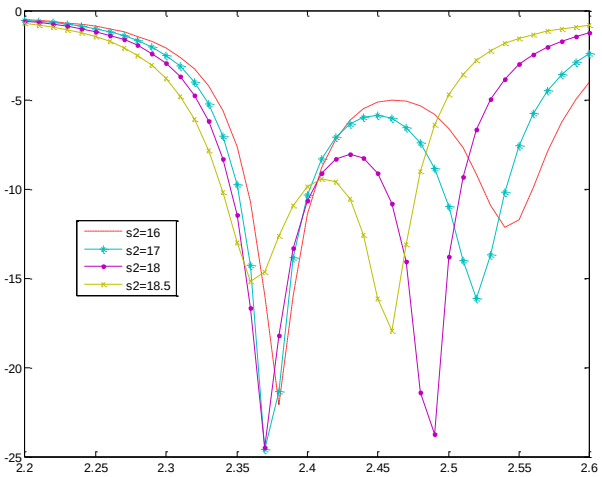

Graphic 4.7 R.L. for different slot-2 positions

4.2 Results

Choosing a separation of $s_2 = 18.5$ mm, we only need to adjust the feed position to match the input impedance.

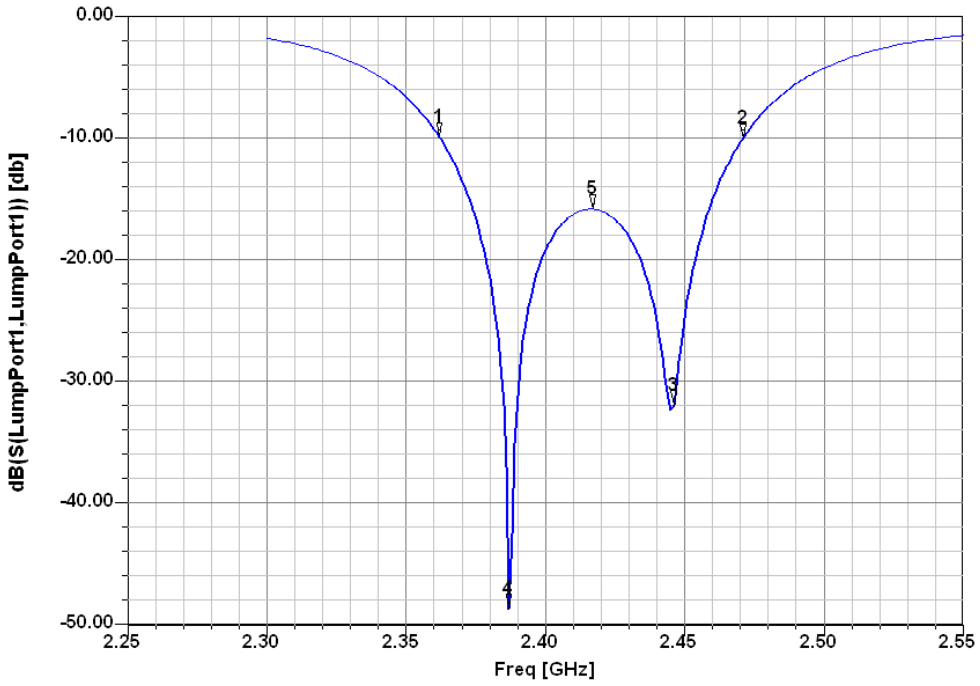

Graphic 4.8 R.L. for the final triangular patch

As we can observe in Graphic 4.8, the final antenna has a bandwidth of 4.6% (110 MHz) which extends from 2.36 GHz (marker 1) until 2.47 (marker 2). The first resonance frequency occurs at 2.385 GHz (marker 4, R.L -48.67 dB). The second resonance frequency occurs at 2.445 GHz (marker 4, R.L. -31.93 dB). In the worst case, that is, the transition between both resonant frequencies, a return loss of -15.85 dB is achieved (at 2.42 GHz, marker 5). Other results are depicted below.

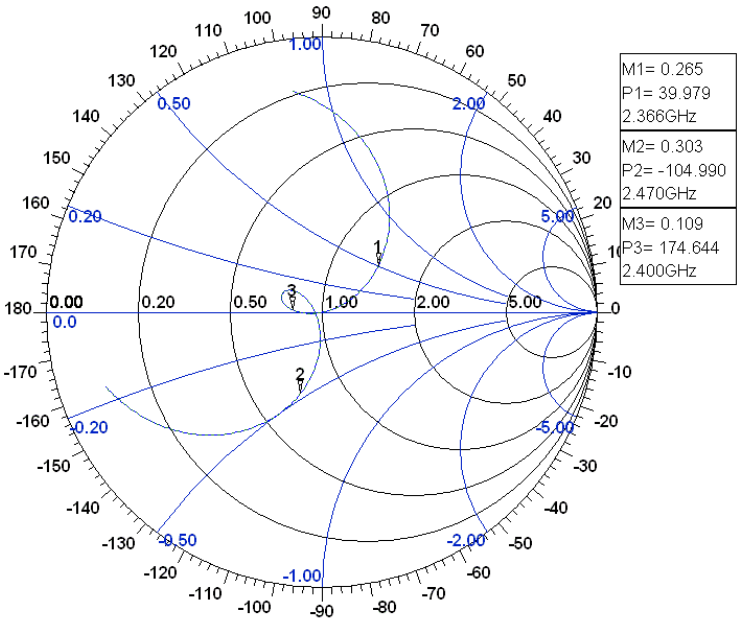

Smith Chart 4.1Patch Input Impedance

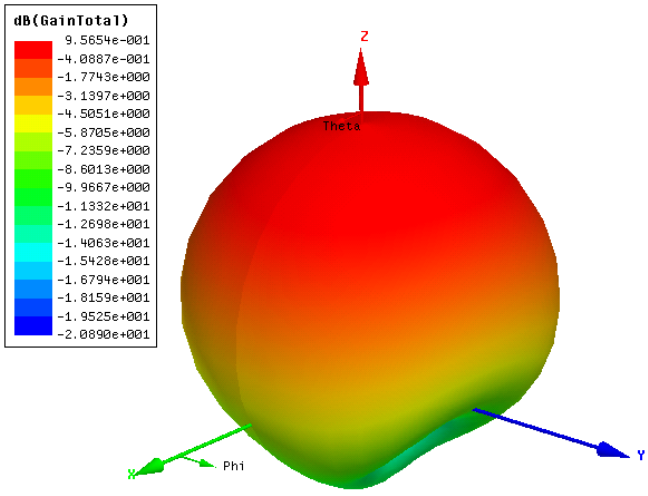

Figure 4.9: Radiation Pattern

CHAPTER V. MIMO ANTENNAS

Until now, we have been analyzing rectangular and triangular patch antennas, as well as a brief introduction to MIMO systems. In this last chapter, the design of MIMO antenna configurations is carried out by using the broadband triangular patch from the previous chapter.

In the first part of the chapter, different designs are simulated. In particular, 2, 4 and 6-port MIMO antennas are designed and the simulation results are included. After that, some of the simulations are chosen for construction and test.

For MIMO antenna design, two kinds of measurements need to be considered. They are conventional antenna performance characteristics and the potential channel capacity. For MIMO communications, the two main impairments that an antenna can imply are related to the effect of the mutual coupling and small antenna size.

5.1 Antenna Simulation

All designs are simulated with *HFSS™ v10* as in previous cases in this work. We have analyzed arrays of 2, 4 and 6 element.

5.1.1 Two-Port Antenna Configuration

In the beginning, two different configurations for the 2-array antenna configuration were taken into account (Fig. 4.1 and 4.2). However, only the second configuration was further analyzed mainly because of the reduction in space that the latter implies.

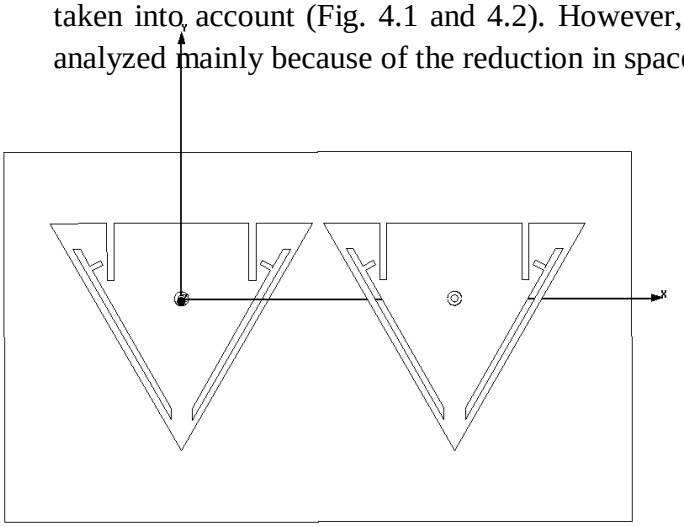

Figure 5.1 First 2-Port Antenna Configuration

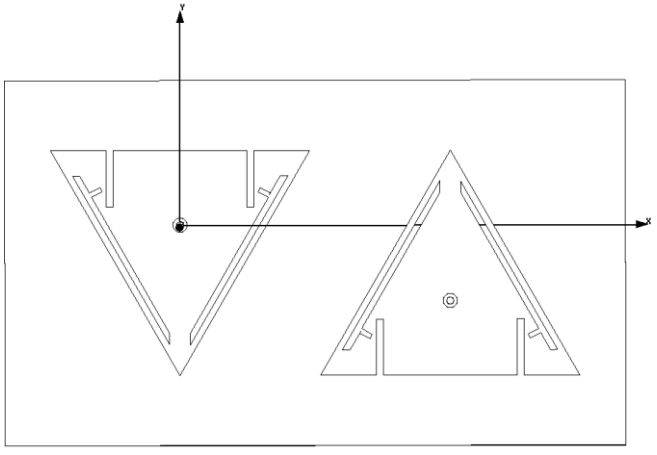

Figure 5.2 Second 2-Port Antenna Configuration

It is interesting to study the coupling between the two patches as we vary the separation between them.

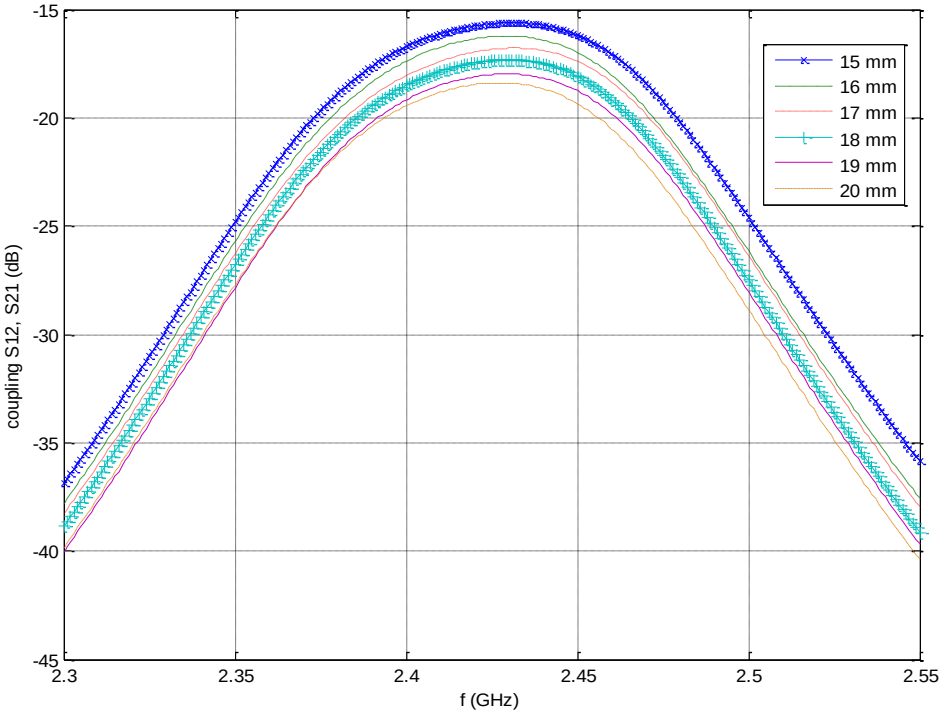

Graphic 5.1 Return Loss for Different Patch Separations

As we can infer from the graphic, coupling deteriorates by 0.6 dB per each millimeter both patches are nearer (Graphic 5.1). In the extremes, we reach a coupling of -16.61 dB and -18.38 when the separation is 15 and 20 mm, respectively.

A comparison between the coupling in the case of an array of two rectangular patches and the triangular case has been performed. As it can be seen in Graphics 4.2 and 4.3, in terms of coupling there is no particular reason for choosing a triangular design instead of a rectangular design. Nevertheless, we should consider the fact that a triangular patch implies less space and it is easier to place in an array configuration.

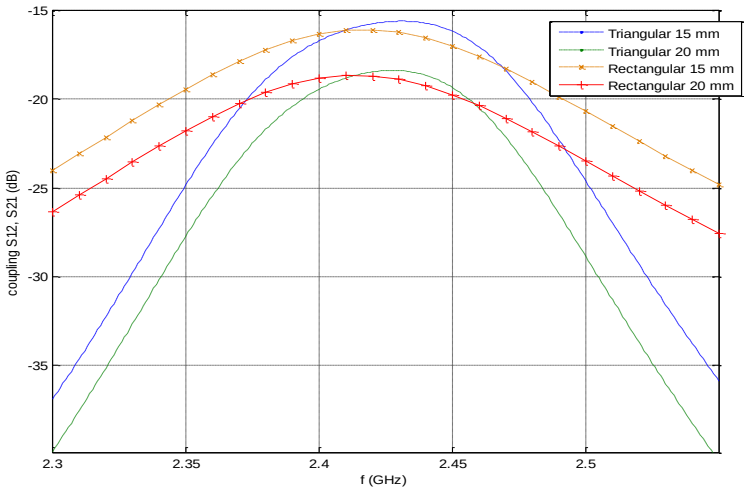

Graphic 5.2 Return Loss for Different Patches

Finally, the best design achieved corresponds to such of two triangular patches inverted and separated 15 mm between them. However, a shift between the patches return loss performance has been detected, which would not fit the initial supposition of the array being completely symmetric.

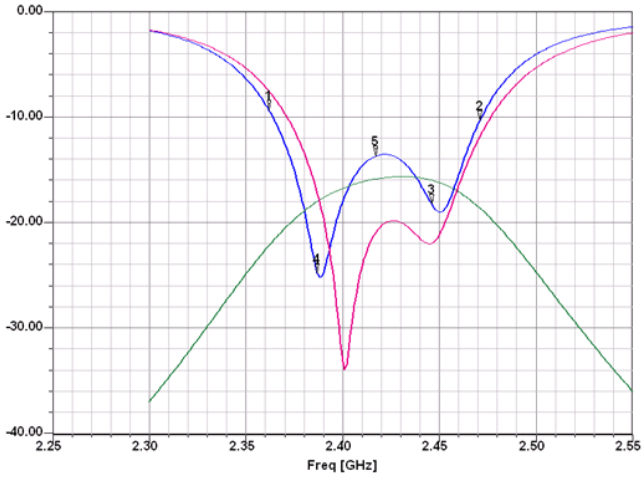

Graphic 5.3 Return Loss

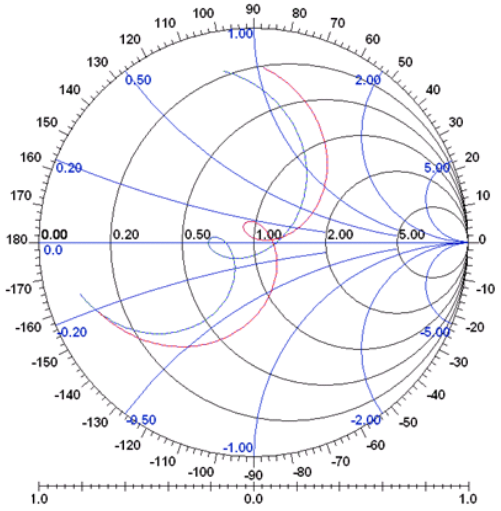

Smith Chart 5.1 Input Impedance

5.1.2 Four-Port Antenna Configuration

As for the four-port antenna, a simple approach has been used: repeating the before-discussed two-patch structure twice.

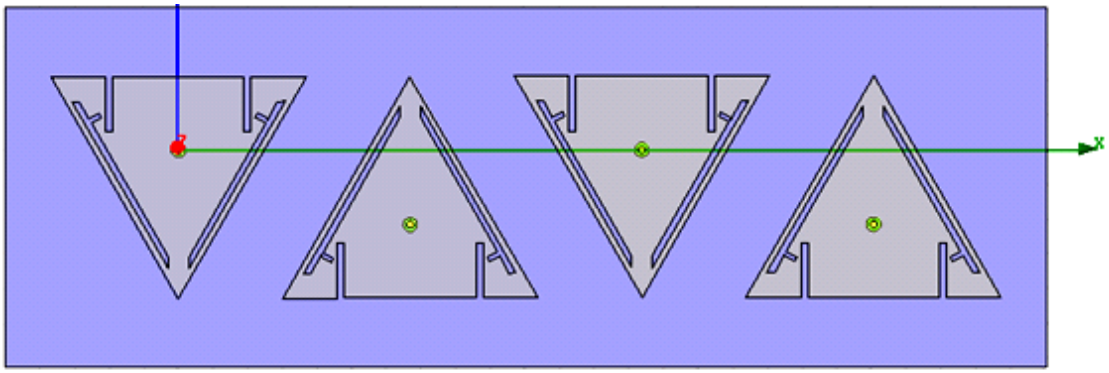

Figure 5.3 Four-Port Antenna

Let us number the patches from left (1) to right (4). Frequency responses of patches 1 and 4 are quite similar (S_{11}, S_{44}), while those of patches 2 and 3 are very related to each other (S_{22}, S_{33}). Return losses are around -40 dB in the resonant frequencies, except from patch 1 that only reaches -30 dB. In the worst case, that is, 2.42 GHz (in the middle of both resonant frequencies), the return loss does not deteriorate beyond -15 dB.

Three different coupling rates can be identified in Figure 5.4. The first coupling rate is produced by patches 2 and 3 as a result of their contact with their neighboring patches (S_{21}, S_{23} and S_{32}, S_{34}). This is set at -16 dB. The opposite pairs show the same results

(S_{12}, S_{43}). The second coupling rate is set at around -24 dB and it is due to the interference between the same patches 2 and 3 with their non-neighboring patches (S_{24}, S_{31}). Again, same results are shown for their opposites (S_{42}, S_{13}). Finally, the most efficient couplings are found to be in the patches which are most remote from each other. Thus, S_{41} and S_{14} are around -32 dB.

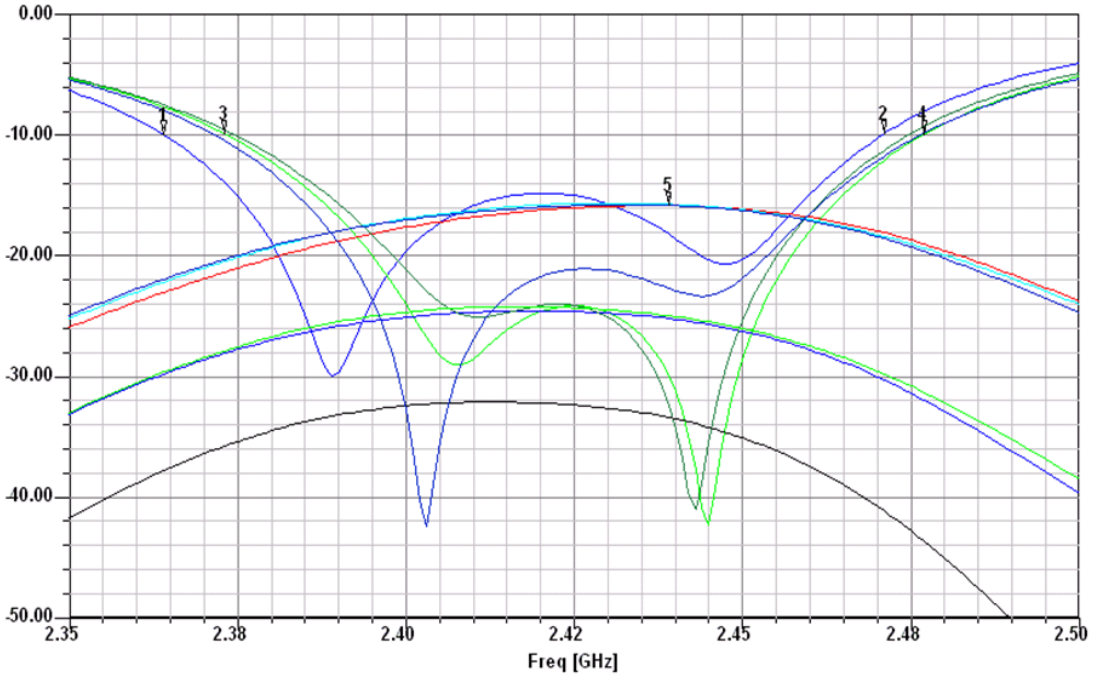

Graphic 5.4 Four-Port Antenna S-Parameters

The input impedance remains constant at about 50Ω in all the bandwidth as we can observe in the Smith Chart.

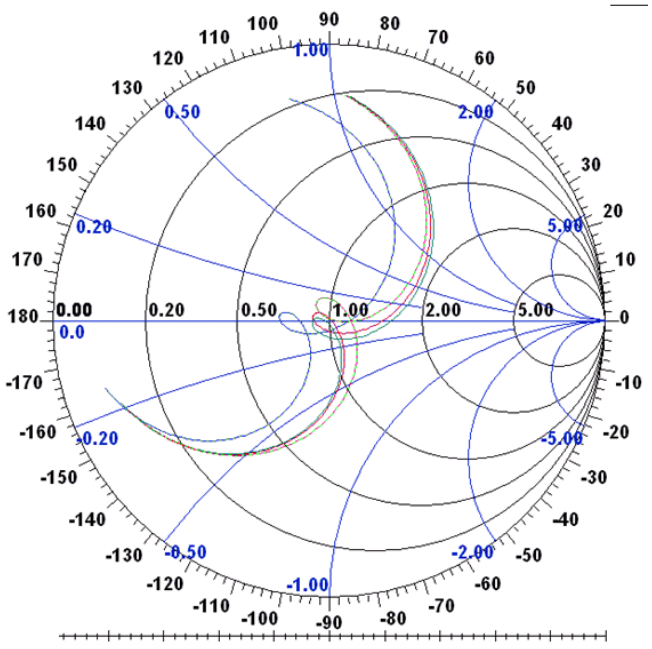

Smith Chart 5.2 Four-Port Antenna Input Impedance

It is also interesting to analyze the radiation patterns. All the related figures are referred to port number one. As it can be noticed from the 3-D radiation pattern, the total gain achieved is not high at all (only -0.26 dB). Besides, the radiation pattern shows to be quite uniform and pointing in the vertical direction and the back lobe is found to be quite small.

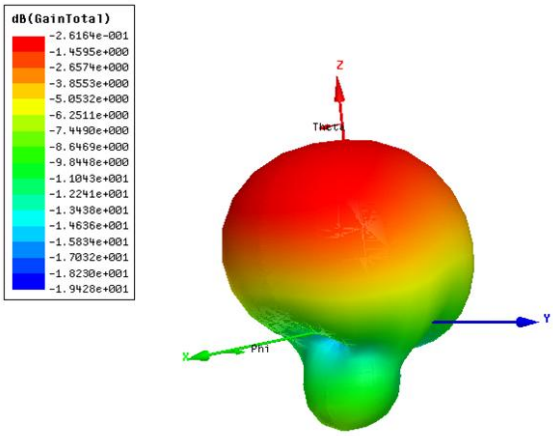

Figure 5.4 3-D Radiation Pattern

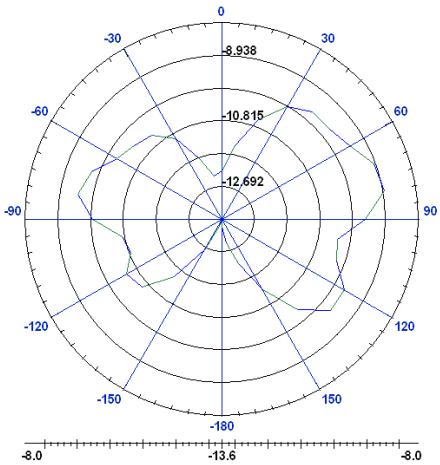

Figure 5.5 XY Radiation Pattern

Figure 5.6 ZY Radiation Pattern

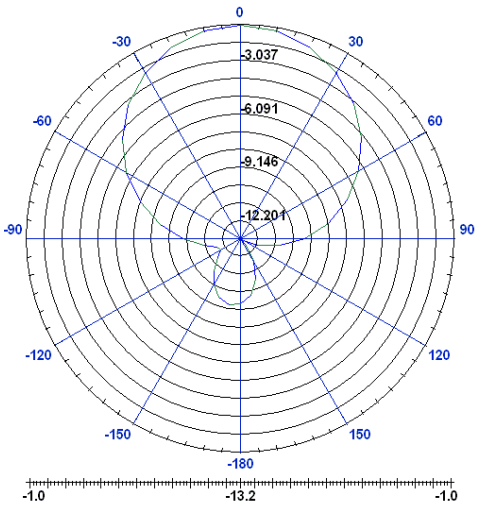

Figure 5.7 ZX Radiation Pattern

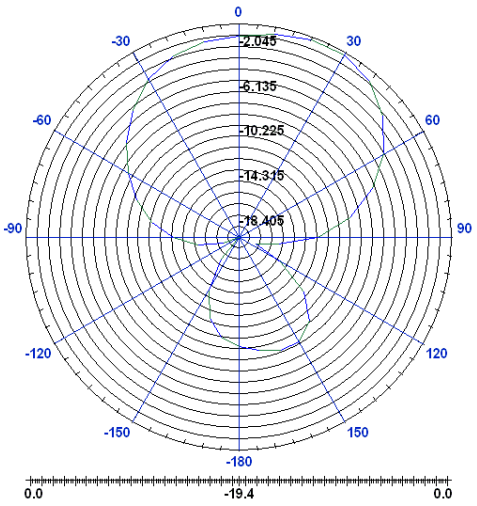

5.1.3 Six-Port Antenna Configuration

The last configuration that has been simulated and analyzed is a six-port antenna configuration. All the patches are placed in a way they are all pointing to the center of the antenna. In this way, the triangular patch has thus demonstrated its capability of high integration.

The six-port antenna functions from 2.38 GHz until 2.45 GHz, which is the range the return losses for each individual patch (S_{ii}) goes below -10 dB. Concerning the coupling, two rates are mainly differentiated. In the first place, the coupling rate which occurs because

of the proximity of a patch with its neighbors is at around -12 dB ($S_{i,i\pm1}$ with *i=1,2,3,4,5,6*). The other coupling rate located at around -25 dB is produced by the interference between more distant elements (S_{13}, S_{14}, S_{15}, S_{26}, S_{24}, S_{25}, S_{31}, S_{35}, S_{35}, S_{36}, S_{42}, S_{46}, S_{41}, S_{53}, S_{51}, S_{52}, S_{63}, S_{64} and S_{62}).

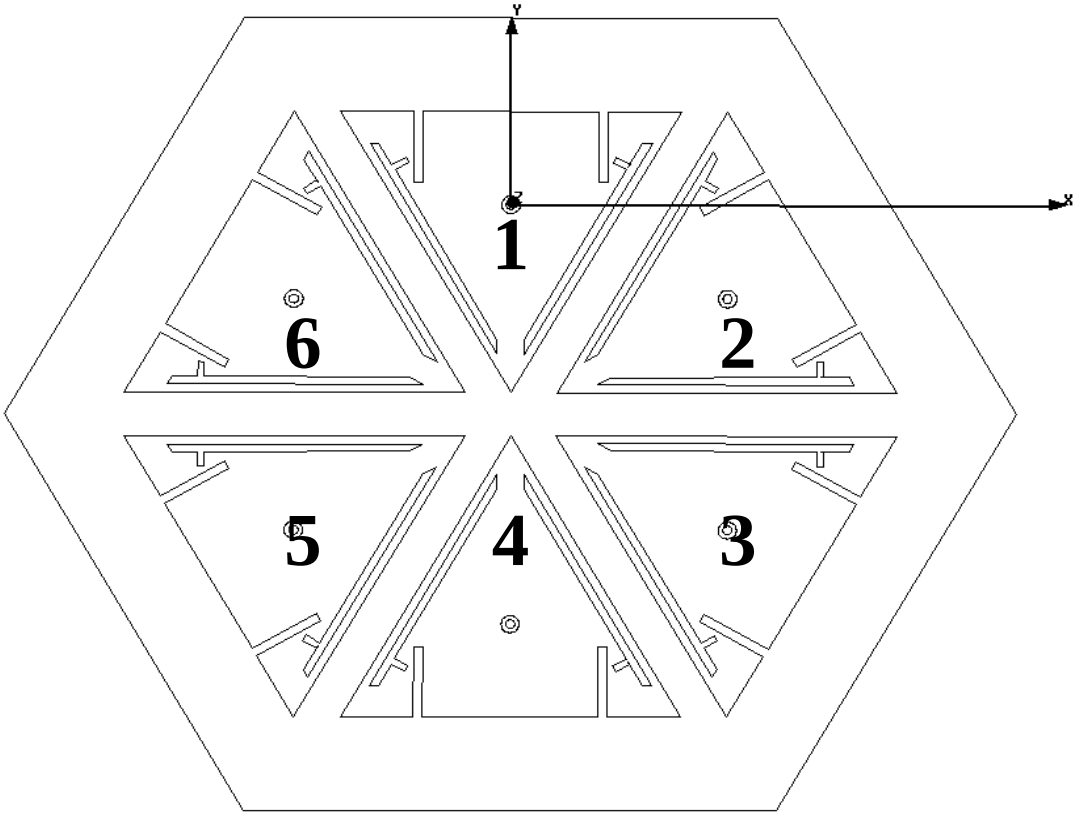

Figure 5.8 Six-Port Antenna Design

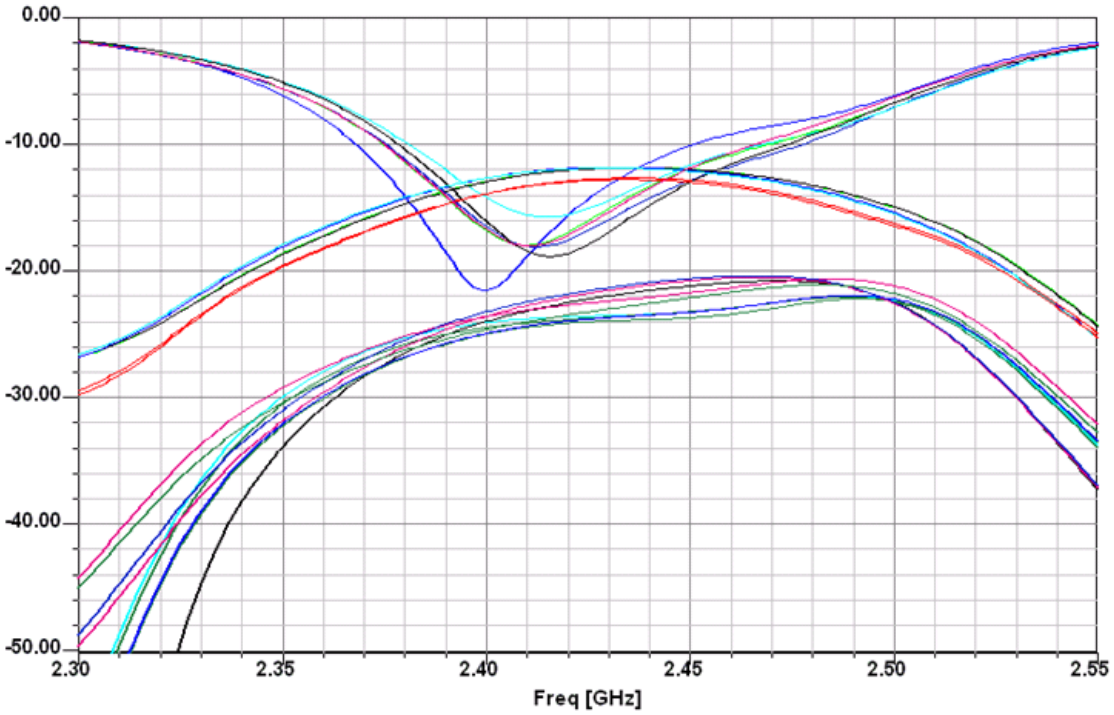

Figure 5.9 Six-Port Antenna Frequency Response (R.L. and Couplings)

The input impedance is also maintained during all the bandwidth of the antenna, although it has deteriorated a little in respect of the four-port case:

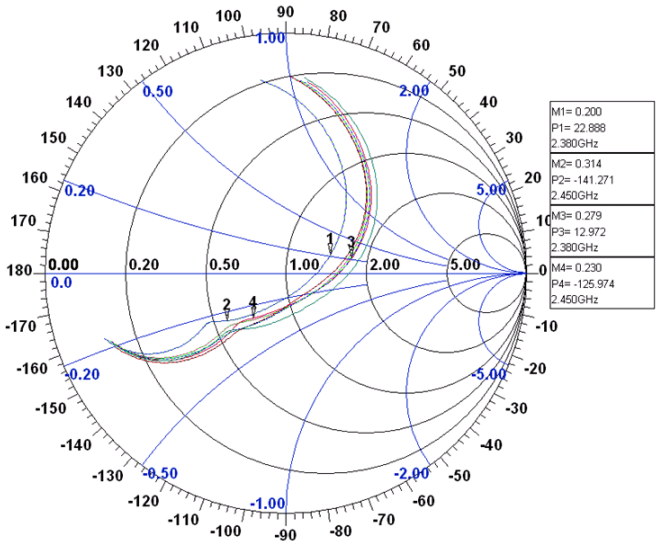

Smith Chart 5.3 Six-Port Antenna Input Impedance

With respect to the radiation patterns, all the characteristics found in the four-port configuration have been maintained. Again, the most remarkable characteristic is the low gain attained.

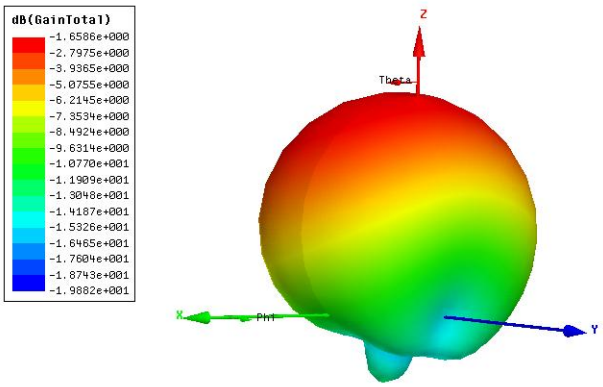

Figure 5.10 3-D Radiation Pattern

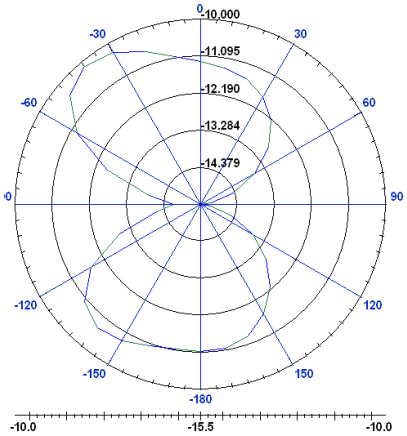

Figure 5.11 XY Radiation Pattern

Figure 5.12 ZY Radiation Pattern

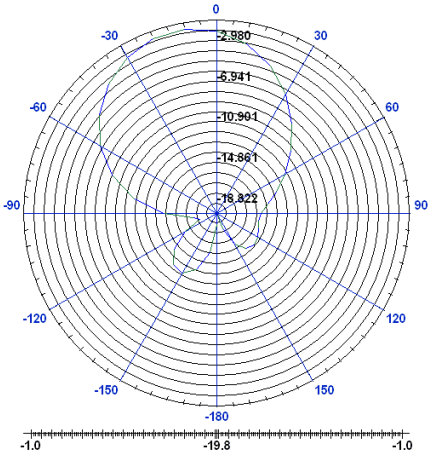

Figure 5.13 ZX Radiation Pattern

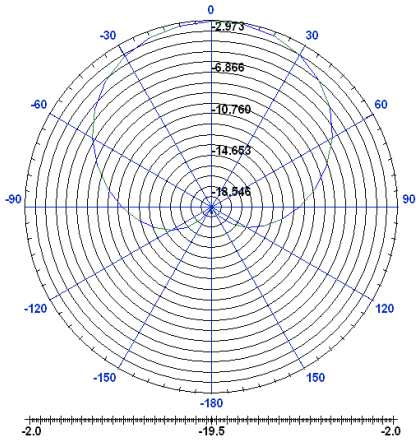

5.2 Four-Port Antenna Configuration

The first antenna which has actually been constructed is the four-port antenna.

The chosen substrate has been the FR-4. This material for PCBs faces a number of limitations. These are due to the treater-based manufacturing process used to produce the substrate from which PCBs are manufactured. Specifically, treaters tend to produce material which suffers from inclusions (air bubbles) and striations (longitudinal air bubbles) as well a deformation of the glass cloth. These imperfections can lead to conductive anodic filaments (CAFs) (caused by electrochemical migration), problems with consistent dielectric constant (dK) (due to resin-rich resin-poor areas) and yield issues (broken connections on the PCB) when a PCB and its components is re-flow soldered. FR-4 is acceptable for signals up to around 2 GHz, depending on the application. (Loss and crosstalk will increase, especially if the same FR-4 board carries multiple high-frequency signals.) Other materials, such as the Rogers 4003 board, provide superior electrical characteristics at higher frequencies. Therefore, choosing FR-4 is mainly a balance of cost and performance. On the other hand, this material will suppose a low antenna efficiency.

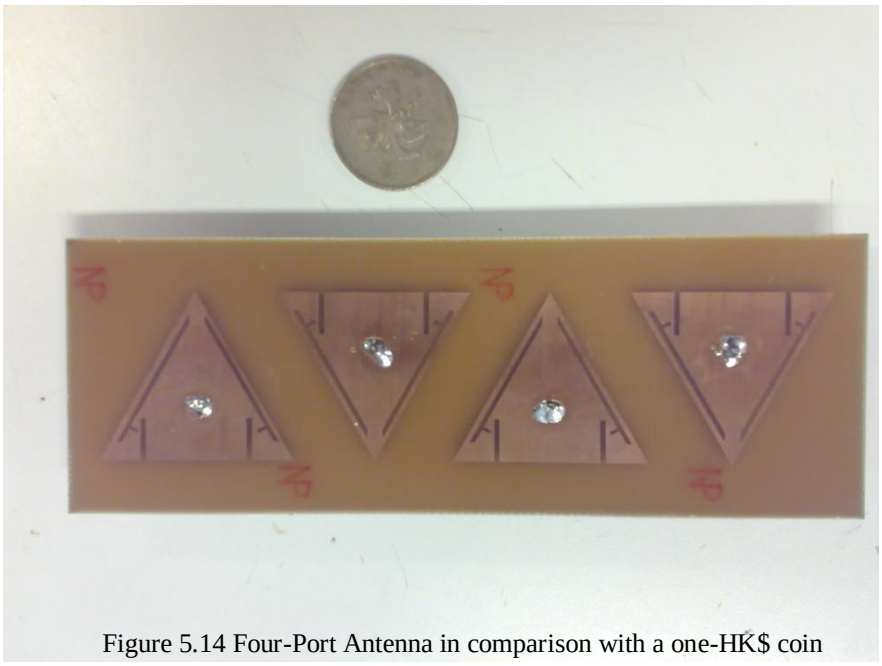

Figure 5.14 Four-Port Antenna in comparison with a one-HK$ coin

For MIMO antenna design, two kinds of measurements need to be considered. They are conventional antenna performance characteristics and also the potential channel capacity.

The measured *S*-parameters of the proposed antenna structure are shown in Fig.5.15. They were obtained with a four-port Vector Network Analyzer (Rohde & Schwarz, ZV8) and therefore, the mutual couplings between all 4 ports are all measured simultaneously. The results are in good agreement with the *HFSS* simulations. The antennas operate from 2.39 GHz to 2.49 GHz, if the impedance bandwidth requirement is less than -10 dB.

The measured radiation patterns of the proposed antenna are given in Figure 5.16, which are measured in an Anechoic Chamber. During each measurement, only one port is connected to the Vector Analyzer, while the other three ports are terminated by 50 Ω. The measured gain is, as commented before, really low (-1.14 dB). However, we should add some 0.5-1 dB to the mentioned gain as the cable introduced to make the measurements is not included in the initial calibration.

Only the data related to the first and second patches are included, since patches three and four are supposed to be equal to ports two and one, respectively.

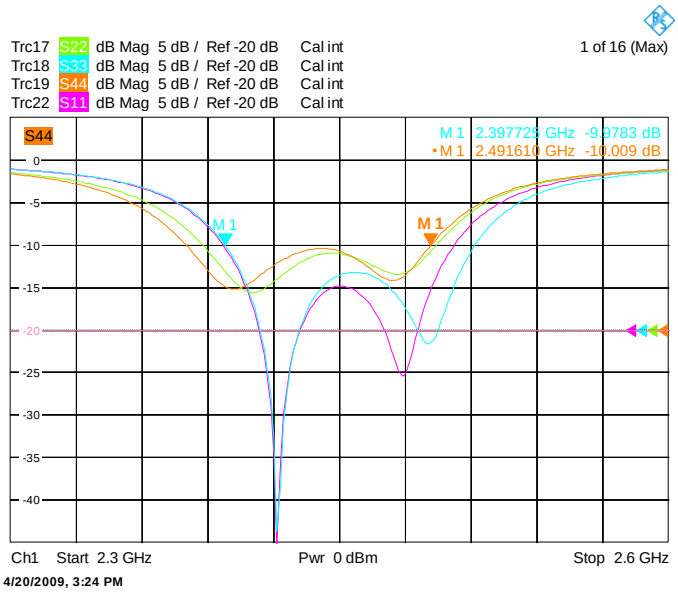

Figure 5.15 3-D Return Loss

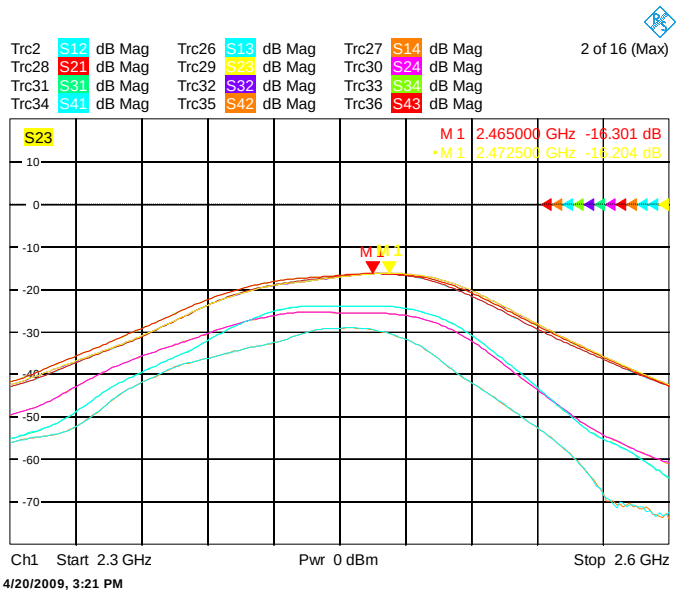

Figure 5.16 Coupling

Figure 5.17 Impedance

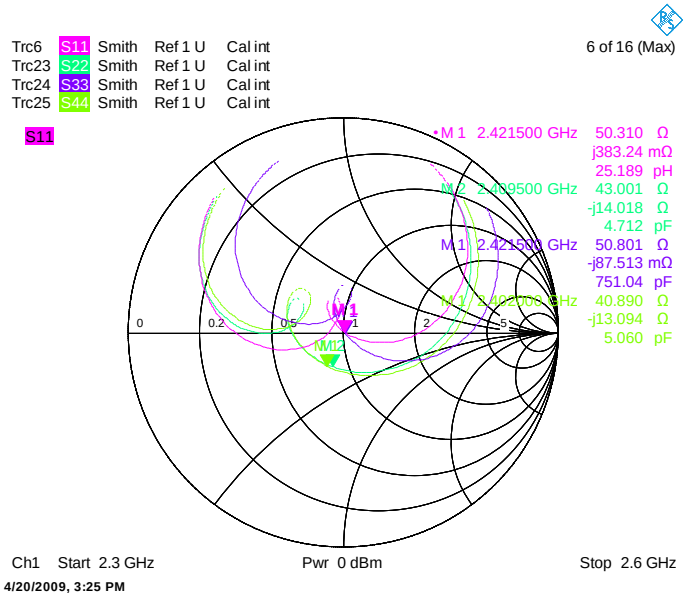

Notable Markers:

Fig.5.15:
- M1: -10 dB @ 2.39 GHz
- M1: -10 dB @ 2.49 GHz

Fig.5.16
- M1: -16.3 dB @ 2.465 GHz

Fig.5.17
- M1: 50.30 Ω + j383 mΩ @ 2.42 GHz
- M1: 43.00 Ω – j14.01 Ω @ 2.40 GHz
- M1: 50.80 Ω + j87.51 mΩ @ 2.42 GHz
- M1: 40.89 Ω – j13.09 Ω @ 2.40 GHz

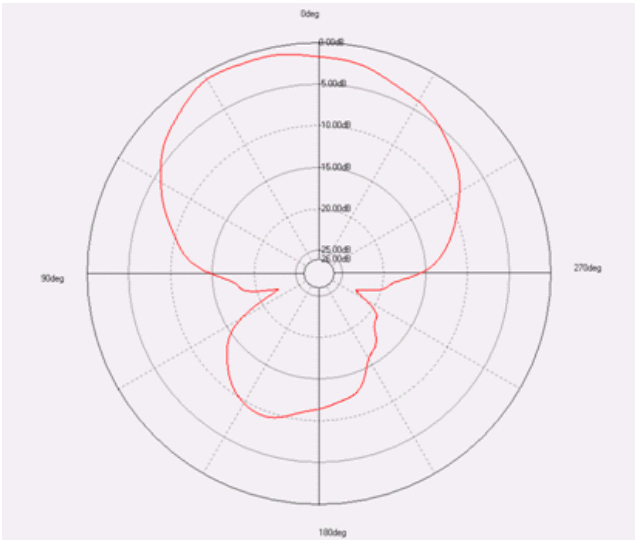

Figure 5.18 Port 1 ZX-Plane

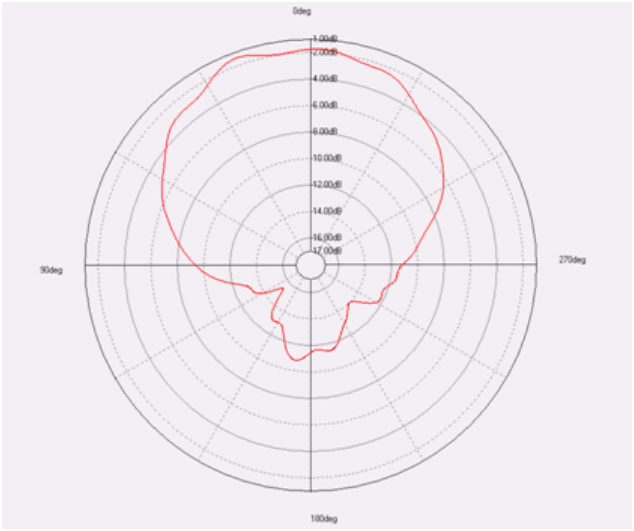

Figure 5.19 Port 1 ZY-Plane

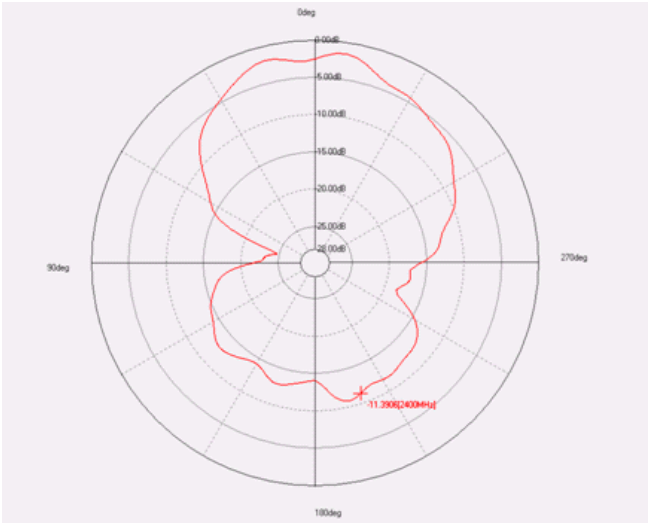

Figure 5.20 Port 2 ZX-Plane

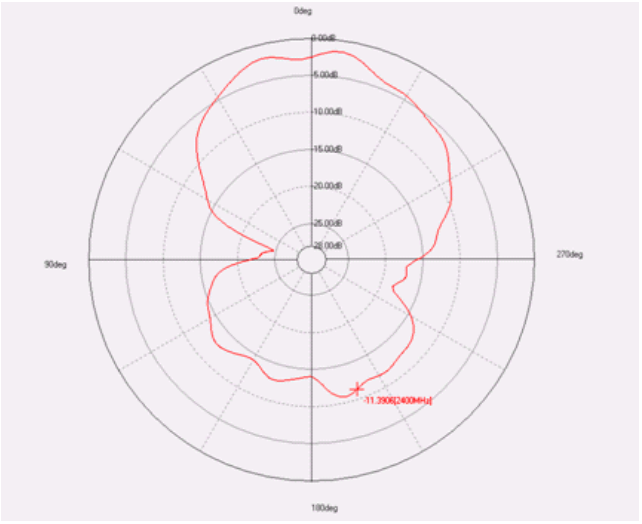

Figure 5.21 Port 2 ZX-Plane

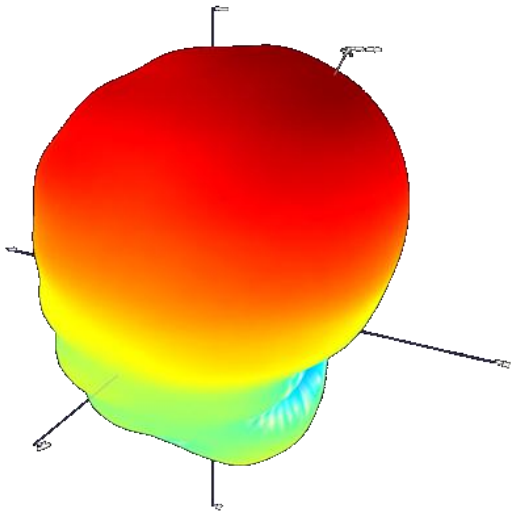

Figure 5.22 Port 1 Radiation Pattern

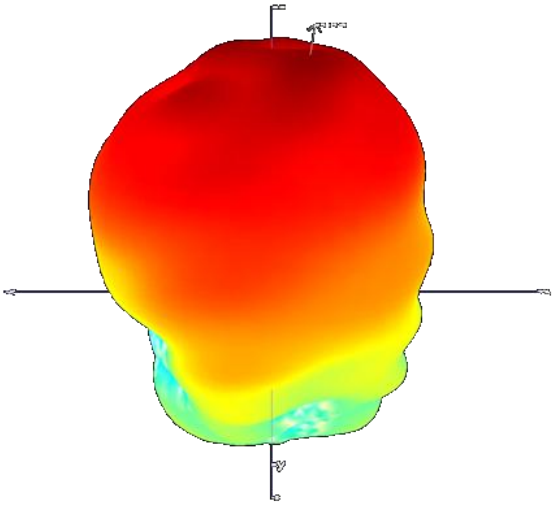

Figure 5.23 Port 2 Radiation Pattern

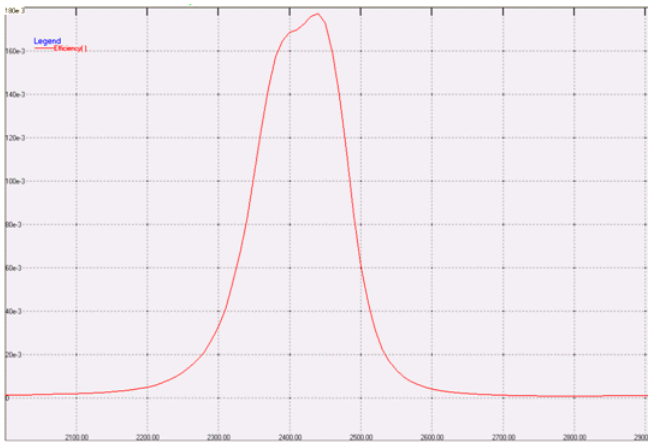

Figure 5.24 Port 1 Gain

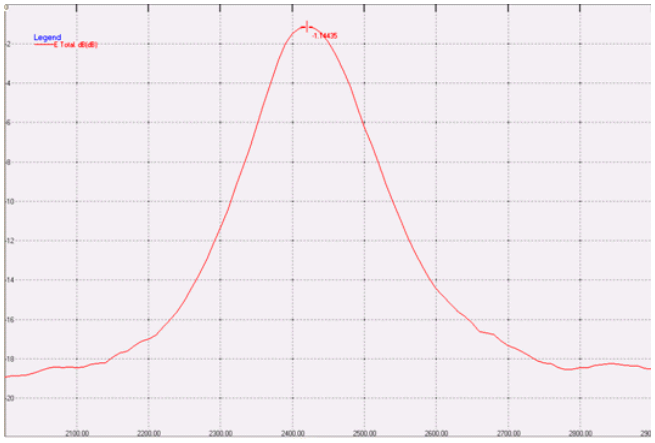

Figure 5.25 Port 2 Gain

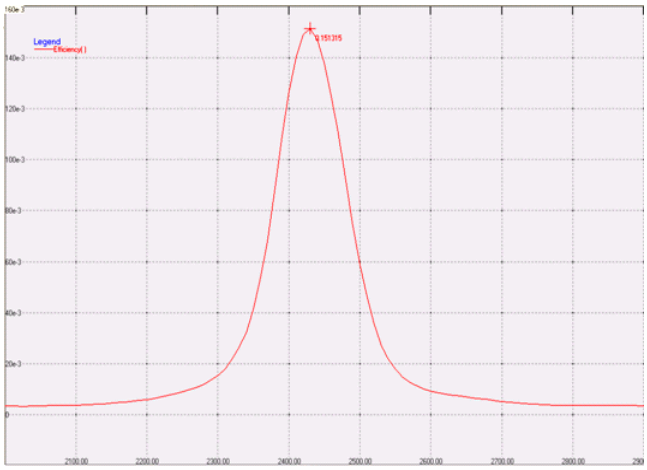

Figure 5.26 Port 1 Efficiency

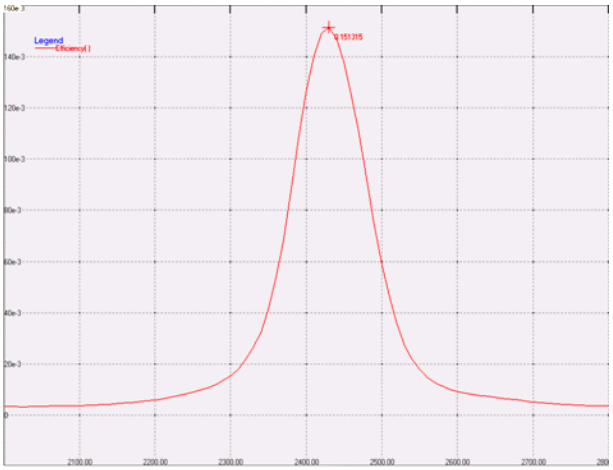

Figure 5.25 Port 2 Efficiency

One application for this antenna is in MIMO wireless communication systems. It is therefore important to try and measure or estimate the capacity that is possible for our four-port antenna so that the effect of the mutual coupling and small antenna size can be observed. Here we experimentally measure the capacity using our 4×4 testbed. The testbed design is described in [40] and provides us with an accuracy of approximately $\pm 2\%$ at 2.48 GHz. From these estimates we can then determine the actual flat fading MIMO capacity.

The procedure is laid out in the following steps:

1. Allow testbed to warm up for at least 5 min.
2. Synchronize signal sources with a cable
3. Number cables so the same ones are used with each Rx-Tx pair every time
4. Number female through connectors

5. Long end of female through connector is connected to Rx side
6. Set Tx signal source power to 0dBm
7. Push button to synchronize transmitter m-sequences
8. Setup acquisition board
   a. +/-0.2V range
   b. 400KS/s samples per second
   c. Collect 1 second sets at 400 KS samples (8x400 KS)
9. Calibrate the system by first connecting the 4 transmit outputs to the 4 receive inputs by the 4-to-1 and 1-to-4 combiner and splitter arrangement.
10. Acquire measurements for 0.1 second and save as start calibration
11. The MIMO measurement system is now ready use after connecting back the antennas
12. After all measurements are complete perform a final calibration so that we can make certain the testbed has been operating correctly before and after the measurement program

After getting the results from MIMO test bed we export the data to MATLAB program for better analysis and comparison on Tx, Rx co-relation coefficients, power (dB) and most importantly the channel capacity. The above measurements are carried out in a comparatively fast fading channel with the designed antenna connected to MIMO transmitter (similar results are expected for transmitter and receiver positions) and the receivers are simple dipole antennas. To ensure these channel conditions, the measurements have been taken while the transmitter antenna was in movement.

The most interesting results we obtain with this method are the correlation matrix and the graphic that shows the capacity improvement that the MIMO system offers:

$$tx\ correlation = \begin{bmatrix} 1 & 0.35132 & 0.33539 & 0.48962 \\ 0.35132 & 1 & 0.2103 & 0.15102 \\ 0.33539 & 0.2103 & 1 & 0.08483 \\ 0.048962 & 0.15102 & 0.08483 & 1 \end{bmatrix}$$

$$rx\ correlation = \begin{bmatrix} 1 & 0.62977 & 0.13774 & 0.15439 \\ 0.62977 & 1 & 0.70008 & 0.071713 \\ 0.13774 & 0.7008 & 1 & 0.59029 \\ 0.15439 & 0.071713 & 0.59029 & 1 \end{bmatrix}$$

Finally, we can easily observe the increase in the channel capacity in the next figure:

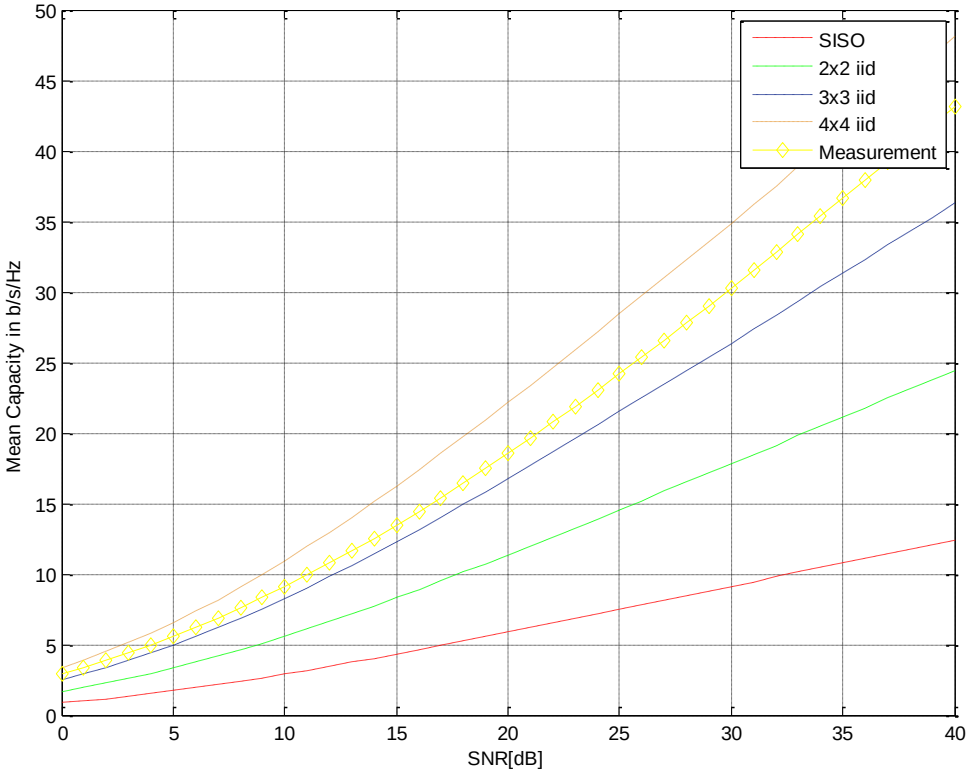

Figure 5.27 Capacity achieved vs. SNR

CHAPTER VI. CONCLUSION

As we have seen, multiple-input multiple-output wireless communications provides significant increases in capacity without requiring increases in transmitting power or spectrum. Furthermore, microstrip technology has demonstrated its capability of creating small-size antenna array which can be used for MIMO communications.

In this report, we aimed to show **a method to implement a MIMO communication system using microstrip technology**. To show this, we reviewed aspects of MIMO communication systems, studied different aspects of the microstrip patch antenna, especially regarding the rectangular and triangular patches. Finally, we designed different antennas: dual-frequency, broad-band and array configurations, all of them based on the triangular patch.

The finalized design corresponds to an array of broad-band triangular patches working at 2.4 GHz with a bandwidth of around 100 MHz, which can be used in MIMO systems. It has been demonstrated that the capacity of the array configuration is far better than the SISO system.

However, we should consider future developments:

- Dual frequency behavior to adapt the antenna to any kind of WLAN 802.11.
- Gain increase.
- Further antenna dimension reduction.

References

1.Wiesbeck, W., Kuhnet, C., Sörgel, W., *Smart Antennas for MIMO Applications,* Institut für Höchstfrequenztechnik und Elektronik Universität Karlsruhe, Germany

2. Biglieri, E., "Chapter I. Introduction", *MIMO Wireless Communications,* Cambridge University Press, Cambridge, 2007

3. Holma, H., Toskala, A., *WCDMA for UMTS,* John Wiley & Sons, New York, 2000

4. Tsoulos, G., *MIMO System Technology for Wireless Communications,* Boca Ratón, Florida, USA, 2006

5. Shiu, D.S., Foschini, J., Gaus, J., Kahn, J.M., "Fading Correlation and its Effects on the Capacity of Multi-Element Antenna System", *IEEE Trans. on Com.,* 48, 502, 2000

6. Telatar, I.E., "Capacity of Multi-Antenna Gaussian Channels", *European Trans. on Telecom.,* Vol. 10, No. 6, December 1999

7. Paulraj, A., Nabar, R., Gore, D., *Introduction to Space-Time Wireless Communications,* Cambridge University Press, Cambridge, 2003

8. Foschini, G.J., "Layered Space-Time Architecture for Wireless Communications in a Fading Environment When Using Multi-Element Antennas", *Bell Labs Tech.,* Autumn 1996

9. Proakis, J.G., *Digital Communications, 4th Ed.,* Chapter 2, McGraw-Hill, New York, 1983

10. Verme, R., Mahajan, S., Rohila, V., "Classification of MIMO Channel Models", *16th IEEE International Conference on Networks 2008 (ICOV 2008),* December 2008

11. Grieg, D.D., and Englemann, H. F., "Microstrip: A New Transmission Technique for the Kilomegacycle Range," *Proceedings of The IRE,* 1952, Vol. 40, No. 10, pp. 1644–1650

12. Deschamps, G.A., "Microstrip Microwave Antennas," *The Third Symposium on The USAF Antenna Research and Development Program,* University of Illinois, Monticello, Illinois, October 18-22, 1953

13. Gutton, H., and Baissinot, "Flat Aerial for Ultra High Frequencies," French Patent no. 703113, 1955

14. James,R.J. and Hall,P.S, *Handbook of Microstrip Antennas,* Eds., Peter Pereguinus, London, U.K., 1989

15. Greg,G., Bhartia,P., Bahl,I. and Ittipiboon,A., *Microstrip Antenna Design Handbook,* Artech House, London

16. Licul, S., Petros, A., and Zafar, I., "Reviewing SDARS Antenna Requirements," *Microwaves & RF* September 2003

17. US Patent No: US 6,307,525 B1

18. James,R.J. and Hall,P.S, *Handbook of Microstrip Antennas,* Eds., Peter Pereguinus, London, U.K., 1989

19. Greg,G., Bhartia,P., Bahl,I. and Ittipiboon,A., *Microstrip Antenna Design Handbook,* Artech House, London

20. Balanis, C.A., *Antenna Theory – Analysis and Design,* Eds.John Wiley & Sons, INC., USA, 1982

21. Carver, K.R. and Mink, J.W., "Microstrip Antenna Technology", *IEEE Trans. on Antenna and Propagation,* Vol.AP-29, No.1, January 1981

22. Pozar, D.M., "Microstrip Antennas", *Proceedings of the IEEE,* Vol.80, No.1, January 1992

23. Kara, M., "Effective Permittivity of Rectangular Microstrip Antenna Elements with Various Thickness of Substrates", *Microwave and Opt. Tech. Letters,* Vol.10, November 1995

24. Kara, M., "Empirical Formulae for the Computation of the Physical Properties of Rectangular Microstrip Antenna Elements with Thick Substrates", *Microwave and Opt. Tech. Letters,* Vol.14, February 1997

25. Kara, M., "Design Considerations for Rectangular Microstrip Antenna Elements with Various Substrate Thicknesses", *Microwave and Opt. Tech. Letters,* Vol.19, No.2, October 1998

26. Basilio, I.L., Khayat, M.A., Williams, J.T. and Long, S.A., "The Dependence of the Input Impedance on Feed Position of Probe and Microstrip Line-Fed Patch Antennas", *Microwave and Opt. Tech. Letters,* Vol.49, No.1, January 2001

27. Guney, K., "Simple and Accurate Formulas for the Physical Dimensions of Rectangular Microstrip Antenna with Thin and Thick Substrates", *Microwave and Opt. Tech. Letters,* Vol.44, No.3, February 2005

28. Akdagli, A., "A Closed-Form Expression for the Resonant Frequency of Rectangular Microstrip Antennas", *Microwave and Opt. Tech. Letters,* Vol.49, No.8, August 2007

29. Akdagli, A., "CAD Formular for Patch Dimensions of Rectangular Microstrip Antennas with Various Substrate Thicknesses", *Microwave and Opt. Tech. Letters,* Vol.49, No.9, September 2007

30. Siddiqui, J.Y., Guha, D., "Applications of Triangular Microstrip Patch: Circuit Elements to Modern Wireless Antenna", *Microwave Review,* Vol.13, No.1, June 2007

31. Hassani, H.R., Mirshekar-Syahkal, D., "Analysis of Triangular Patch Antennas Including Randome Effects", *IEEE Proc. H Microwave and Prop.,* Vol.139, No.3, pp.251-256, June 1992

32. Tetuko, J., Sumantyo, S., Ito, K., Takahashi, M., "Dual-band Circularly Polarized Equilateral Triangular Patch Array Antenna for Mobile Satellite Communications", *IEEE Trans. on Antenna and Propagation,* Vol.53, No.11, pp.3477-3485, Nov. 2005

33. Chen, W., Luk, K.-M. and Dahele, J.S., "Theoretical and Experimental Studies od the Resonant Frequencies of the Equilateral Triangular Microstrip Antenna", *IEEE Trans. on Antenna and Propagation,* Vol.AP-40, pp.1253-1256, 1992

34. Pahele, J.S., Lee, K.-F., "On the Resonant Frequencies of the Triangular Patch Antenna", *IEEE Trans. on Antenna and Propagation,* Vol.AP-35, No.1, January 1987

35. Güney, K., "Comments on 'On the Resonant Frequencies of the Triangular Patch Antenna' ", *IEEE Trans. on Antenna and Propagation,* Vol.42, No.1, Sept. 1994

36. Lu, J-H., Tang, C-L., Wong, K-L., "Novel Dual-Frequency and Broad-Band Designs of Slot-Loaded Equilateral Triangular Microstrip Antennas", *IEEE Trans. on Antenna and Propagation,* Vol.48, No.7, July 2000

37. Lee, K.F, Luk, K.M., Dahele, J.S., "Characteristics of the Equilateral Triangular Patch Antenna", *IEEE Trans. on Antenna and Propagation,* Vol. 36, November 1987

38. Maci, S., Biffi Gentili, G., "Dual-Frequency Patch Antennas", *IEEE Trans. on Antenna and Propagation,* Vol. 39, No. 6, December 1997

39. Chen, J-S., Wong, K-L., "A Single-Layered Dual-Frequency Rectangular Microstrip Patch Antenna Using a Single Probe Feed", *Microwave and Opt. Tech. Letters,* Vol.11, 2, 1996

40. Chiu, C.Y., Cheng, C.H., Wan, Y.S., Murch, R.D., "Design of a Flat Fading 4 x 4 MIMO Testbed for antenna characterization using a modular approach", *IEEE Wireless Commun. Netw. Conf.,* Hong Kong, March 2007

41. Chiu, C.Y., Cheng, C.H., Murch, R.D., "Reduction of Mutual Coupling Between Closely-Packed Antenna Elements", *IEEE Trans. on Antenna and Propagation,* Vol. 55, No. 6, June 2007

43. Zhang, H., Wang, Z., Yu, J., Huang, J., "A Compact MIMO Antenna for Wireless Communication", *IEEE Antenas and Propag. Magazine,* Vol.50, No.6, December 2008

44. Chiu, C.Y., Yan, J-B., Murch, R.D., "24-Port and 36-Port Antenna Cubes Suitable for MIMO Wireless Communications", *IEEE Trans. on Antenna and Propagation,* Vol. 56, No. 4, April 2008

45. Murch, R.D., Letaief, K.B., "Antenna Systems for Broadband Wireless Access", *IEEE Communicaitons Magazine,* April 2002